

A space-time smooth artificial viscosity method with wavelet noise indicator and shock collision scheme, Part 1: the 1- D case.

Raaghav Ramani
Department of Mathematics
University of California
Davis, CA 95616 USA
rramani@math.ucdavis.edu

Jon Reisner
Los Alamos National Lab
XCP-4 MSF605
Los Alamos, NM 87544
reisner@lanl.gov

Steve Shkoller
Department of Mathematics
University of California
Davis, CA 95616 USA
shkoller@math.ucdavis.edu

March 4, 2019

Abstract

In this first part of two papers, we extend the C -method developed in [40] for adding localized, space-time smooth artificial viscosity to nonlinear systems of conservation laws that propagate shock waves, rarefaction waves, and contact discontinuities in one space dimension. For gas dynamics, the C -method couples the Euler equations to a scalar reaction-diffusion equation, whose solution C serves as a space-time smooth artificial viscosity indicator.

The purpose of this paper is the development of a high-order numerical algorithm for shock-wall collision and bounce-back. Specifically, we generalize the original C -method by adding a new collision indicator, which naturally activates during shock-wall collision. Additionally, we implement a new high-frequency wavelet-based noise detector together with an efficient and localized noise removal algorithm. To test the methodology, we use a highly simplified WENO-based discretization scheme. We show that our scheme improves the order of accuracy of our WENO algorithm, handles extremely strong discontinuities (ranging up to nine orders of magnitude), allows for shock collision and bounce back, and removes high frequency noise. The causes of the well-known “wall heating” phenomenon are discussed, and we demonstrate that this particular pathology can be effectively treated in the framework of the C -method. This method is generalized to two space dimensions in the second part of this work [41].

Contents

1	Introduction	2
1.1	Using artificial viscosity with conservation laws	4
1.2	Stabilizing shock collision	5
1.3	High-frequency noise	6
1.4	Outline of the paper	6
2	The compressible Euler equations and the original C-method	7
2.1	The conservation laws of gas dynamics	7
2.2	A review of the original C -method	8

3	A new C-method for shock-wall collision	9
3.1	The Euler- C - W system	10
3.2	Boundary conditions for the Euler- C - W system	11
3.3	The WENO- C - W algorithm	11
3.3.1	Discretization of the Euler- C - W system	11
3.3.2	Discretization of boundary conditions and ghost node values	13
3.4	Using WENO- C - W for the Sod shock-wall collision problem	14
3.4.1	An explanation of the temporal bump function $\overline{C}_w(t)$	15
3.4.2	A generalization of our algorithm to shock-shock collision problems	16
4	A wavelet-based noise indicator: the WENO-C-W-N method	17
4.1	Construction of wavelets	18
4.2	High-frequency noise detection	19
4.3	Noise detection in the presence of a shock wave	20
4.4	Noise removal algorithm	21
4.5	The WENO- C - W - N algorithm	22
5	Numerical simulations of classical shock tube experiments	23
5.1	Linear advection	24
5.2	The Sod shock tube problem	25
5.2.1	The wall-heating problem in the Sod shock tube	25
5.2.2	A solution to the wall-heating problem	27
5.2.3	Noise removal with the noise indicator	30
5.2.4	Error analysis and convergence tests	31
5.2.5	Comparison with other schemes	34
5.3	The Noh problem	35
5.4	The LeBlanc shock tube problem	36
5.4.1	Stabilizing shock-wall collision	37
5.4.2	Error analysis and convergence tests	39
5.5	The Peak shock tube problem	41
5.6	The Osher-Shu shock tube problem	43
5.6.1	Noise removal with the noise indicator	43
5.6.2	Stabilizing shock-wall collision for Osher-Shu	47
6	Concluding remarks	47
A	The WENO-u_x and WENO-Noh schemes	48
A.1	WENO- $ u_x $: classical artificial viscosity	48
A.2	WENO-Noh: an artificial viscosity method of Noh	48
B	Calculation of the exact solution post shock-wall collision	49
C	Comparison of optimized-parameter runs with fixed-parameter runs	50

1 Introduction

This is the first in a two-part series of papers, in which we develop a high-order numerical algorithm to simulate compressible fluid flow with shock waves and contact discontinuities, as well as shock-wall collision and bounce-back. In the second part of this series [41], we

treat problems in two space dimensions. In this first part, we begin the development for one-dimensional flows.

The initial-value problem for a nonlinear system of conservation laws in one space dimension is given as

$$\partial_t \mathbf{u}(x, t) + \partial_x F(\mathbf{u}(x, t)) = 0, \quad (1a)$$

$$\mathbf{u}(x, t = 0) = \mathbf{u}_0(x), \quad (1b)$$

where $\mathbf{u}(x, t)$ denotes a vector of conserved quantities, x denotes the space coordinate, and t denotes the time coordinate. Many different physical phenomena can be modeled by (1), including gas dynamics, described by the compressible Euler equations, which shall be the focus of this paper.

It is well known that solutions of (1) can develop finite-time discontinuities, even for smooth initial data \mathbf{u}_0 . In this case, the discontinuities are propagated according to the *Rankine-Hugoniot* conditions (see §2.2). Consequently, it is important to develop robust numerical schemes that can approximate discontinuous solutions. This is a nontrivial task, since approximations to discontinuous solutions usually result in the occurrence of small-scale oscillations, or Gibbs-phenomenon; however, a variety of high-order discretization schemes and techniques have been developed to combat this issue and produce non-oscillatory solutions. In the case of 1-D gas dynamics, the construction of non-oscillatory, higher-order, numerical algorithms such as ENO by Harten, Engquist, Osher & Chakravarthy [16] and Shu & Osher [45], [46]; WENO by Liu, Osher, & Chan [29] and Jiang & Shu [19]; MUSCL by Van Leer [23], Colella [7], and Huynh [17]; or PPM by Colella & Woodward [9] requires carefully chosen *reconstruction* and *numerical flux*.

Such numerical methods evolve cell-averaged quantities; to calculate an accurate approximation of the flux at cell-interfaces, these schemes reconstruct k th-order ($k \geq 2$) polynomial approximations of the solution (and hence the flux) from the computed cell-averages, and thus provide k th-order accuracy away from discontinuities. See, for example, the convergence plots of Greenough & Rider [15] and Liska & Wendroff [25]. Given a polynomial representation of the solution, a strategy is chosen to compute the most accurate cell-interface flux, and this is achieved by a variety of algorithms. Centered numerical fluxes, such as Lax-Friedrichs, add dissipation as a mechanism to preserve stability and monotonicity. On the other hand, *characteristic-type* upwinding based upon exact (Godunov) or approximate (Roe, Osher, HLL, HLLC) Riemann solvers, which preserve monotonicity without adding too much dissipation, tend to be rather complex and PDE-specific; moreover, for strong shocks, other techniques may be required to dampen post-shock oscillations or to yield entropy-satisfying approximations (see Quirk [39]). Again, we refer the reader to the papers [15], [25] or Colella & Woodward [8] for a thorough overview, as well as a comparison of the effectiveness of a variety of competitive schemes.

Majda & Osher [22] have shown that *any* numerical scheme for a problem with discontinuities will suffer from a formal loss of accuracy near the discontinuity. Nonetheless, the use of high-order schemes is imperative for the resolution of finer structures in smooth regions of the flow. Formally high-order WENO schemes (as well as other high-order methods) maintain high-order accuracy in regions away from shocks, but are only first-order accurate at the discontinuity.

In order to ascertain the performance of a method, it is essential to conduct numerical tests for a range of problems with different features of varying complexity. These tests are made precise by calculating error norms of the computed solution relative to either an exact solution (if available), or a highly resolved solution which may be regarded as the exact solution. Proposed numerical algorithms should demonstrate small error norms and close to optimal convergence for a range of test problems. However, due to the fact that different tests can exhibit very different phenomena and features, it is not so surprising that there are a number of situations in which anomalous behavior of solutions is observed, which results in large errors and poor rates of convergence. Examples of such errors are wall-heating, the carbuncle phenomenon, long wavelength instabilities in slow-moving shocks, and non entropy-satisfying “expansion shocks” (see Quirk [39] for further details).

In this paper, we continue the development of the C -method [40], a nonlinear artificial viscosity modification of the Euler equations of gas dynamics, whose numerical discretization by a simple WENO-type (or even central differencing) scheme can stabilize the type of instabilities noted above. As proven in [40], weak solutions of the C -method modification of the Euler equations converge to the unique (entropy) solutions of the Euler equations as the artificial viscosity parameter tends to zero. Herein, we present numerical error analysis and order of accuracy studies for a number of classical shock tube experiments; we show that a highly simplified WENO discretization of the C -method yields highly accurate solutions displaying close to optimal rates of convergence.

For instance, we show that for the Sod problem, our simple WENO-type discretization of the C -method yields smaller errors and faster rates of convergence in the L^1 , L^2 , and L^∞ norms as compared to the same WENO discretization of the unmodified Euler equations. In particular, for the difficult problem of shock-wall collision (to be introduced in §1.2 and developed in §3) for the Sod problem on a grid with 801 cells, we show that the L^1 error with the C -method is 35% of the error without the C -method. Moreover, the order of convergence of solutions is approximately 0.95, which is close to optimal and more than twice the order of convergence when the C -method is not employed. Similar conclusions hold also for the extremely difficult LeBlanc problem, for which we show that the use of the C -method produces L^1 errors that are approximately four times smaller prior to shock-wall collision, and approximately three times smaller post shock-wall collision.

Our quantitative analysis, together with the qualitative observations we make via plot comparison, lead us to conclude that the use of a simple discretization of the C -method provides a flexible, highly accurate scheme that produces solutions with close to optimal rates of convergence for a variety of problems with different features.

1.1 Using artificial viscosity with conservation laws

Artificial viscosity is an effective method for the numerical stabilization of shock waves in gas dynamics; the simplest such regularization of (1) replaces the right-hand side with the linear second-order operator (see, for instance, [20, 50, 11])

$$\beta \Delta x \partial_{xx} \mathbf{u}(x, t), \tag{2}$$

where $\beta = O(1)$ is a constant, and Δx denotes a small asymptotic parameter that, when the term (2) is numerically discretized, represents the grid spacing.

For each such $\beta > 0$, solutions to the regularized conservation law smooth the shock across a small region of width proportional to Δx , and simultaneously prevent small-scale oscillations from corrupting sound waves in numerical simulations; nevertheless, the uniform application of diffusion given by (2) ensures only first-order accuracy of numerical schemes and overly diffuses wave amplitudes and speeds.

In [49], Von Neumann and Richtmeyer replaced the uniform linear viscosity (2) with a nonlinear term given by

$$\beta (\Delta x)^2 \partial_x (|\partial_x u| \partial_x u) , \quad (3)$$

which we shall refer to as *classical artificial viscosity*. Here, $u(x, t)$ represents, in the case of the Euler equations of gas dynamics, the velocity of the fluid. The use of the localizing coefficient $|\partial_x u|$ in (3) concentrates the addition of viscosity to the narrow intervals containing shocks, while maintaining high-order accuracy in regions away from the shock, wherein the solution is smooth. See also Margolin [31] and Mattsson & Rider [32] for a description of the origin and the interpretation of artificial viscosity as a physical phenomenon.

It is now well-known [21, 14] that classical artificial viscosity corrects for the over-dissipation of the linear viscosity (2), and allows for the implementation of numerical methods that are both non-oscillatory at shocks, as well as high-order accurate in smooth regions. On the other hand, the fact that the localizing coefficient $|\partial_x u|$ itself becomes highly irregular in regions containing shocks often results in the failure of such schemes to suppress spurious oscillations. This inadequacy of classical artificial viscosity may be observed with the highly singular phenomenon of shock-wave wall collision. In this case, large amplitude, high frequency, non-physical oscillations appear in the solution post-collision behind the shock curve, and the rough nature of $|\partial_x u|$ in both space and time means that the classical artificial viscosity is often unable to remove such oscillations.

This suggests that a space-time smoothed variant of the localizing coefficient $|\partial_x u|$ might allow for a less oscillatory, more accurate solution profile. We propose the use of the C -method as a means of producing such a localizing coefficient. A similar method is employed by Cabot & Cook [3, 4], who use a high-wavenumber indicator together with a Gaussian filter to produce such a function, though we note that the produced function is only spatially regularized, and not temporally. See also the work of Barter & Darmofal [2], who utilize a PDE-based approach to smooth the localizing function. As we shall explain below, the function $C(x, t)$ will play the role of $|\partial_x u|$; not only will it be a space-time smooth approximation, but it will moreover be an envelope for $|\partial_x u|$, maintaining its highly localized properties while retaining a certain memory of the behavior of the shock wave.

1.2 Stabilizing shock collision

In the context of fixed-grid, explicit, finite-difference schemes, shock-wall collision and bounce-back leads to egregious oscillatory behavior. This is primarily due to the fact that the shock-wall collision causes an immediate change in the sign of the shock speed $\dot{\sigma}(t)$, leading to a discontinuity in $\dot{\sigma}(t)$. Consequently, shock-wall collision is a highly singular phenomenon that requires explicit stabilization. In §3, we introduce a simple modification

of the C -method, which we call the wall C -method, that implements a space-time smooth stabilization for shock-wall collision. This method is then applied to various test cases in §5, with the computed solutions showing excellent agreement with the exact solution post shock-wall collision. Error analysis and convergence tests show that the wall C -method produces solutions with much smaller errors, even for the difficult LeBlanc shock tube problem.

1.3 High-frequency noise

The occurrence of high-frequency, often small amplitude, spurious oscillations (or *noise*) is a common issue in numerical schemes. One cause of this noise is related to the stability (CFL) condition for explicit time-integration methods. A simple method for suppressing such noise is the use of the linear viscosity (2), though, as explained above, this often results in the degradation of the solution in regions without noise. An alternative is to first decompose the solution using a basis of orthogonal *wavelets*, then truncate the decomposition so as to remove the high frequency components (which correspond with noise), though this may be very computationally expensive and, moreover, requires the use of a fully orthogonal basis of wavelets. In §4, we introduce a hybridized version of the two above methods, wherein wavelets are used to accurately locate high frequency noise, and then a linear viscosity is used, via a localized heat equation solver, to remove this noise. This noise detection and removal algorithm is very simple to implement, and is applied to a number of test problems in §5. Error analysis shows that the algorithm improves the accuracy of the solution while retaining the order of convergence; in particular, the algorithm is able to suppress high-frequency noise while preserving the amplitude of lower frequency (physical) sinusoidal waves for the Osher-Shu problem.

1.4 Outline of the paper

In §2.1, we introduce the compressible Euler equations, the corresponding flux, and the Rankine-Hugoniot jump conditions. In §2.2, we review the original C -method, as introduced in [40]. Then in §3, we discuss the problem of shock-wave wall collision, and introduce a novel generalization of the C -method, which relies on a new artificial *wall viscosity* mechanism that suppresses post shock-collision oscillations. We then introduce our WENO- C - W scheme as a discretized version of our new C -method for shock-wall collision. In §4, we present a wavelet based *noise indicator*, that locates regions of noise containing high frequency oscillations on the discretized domain. A noise removal algorithm, based on a localized solution of the heat equation, is then used to remove high frequency oscillations. We then describe our WENO- C - W - N algorithm which adds the noise indicator and noise removal scheme to our WENO- C - W method. Finally, in §5, we demonstrate the efficacy of our method for a number of classical shock tube problems, including the Sod, LeBlanc, Peak, and Osher-Shu tests. We show numerical results and order-of-accuracy studies, and in the process, we explain the cause and solution to the wall-heating problem. In Appendix A, we describe two WENO schemes that we use for comparison purposes: the first couples WENO with classical artificial viscosity, while the second couples WENO with Noh's artificial viscosity operator, designed specifically for the case of shock-wall collision and the wall-heating phenomenon.

2 The compressible Euler equations and the original C -method

2.1 The conservation laws of gas dynamics

The compressible Euler equations on a 1- D spatial interval $x_1 \leq x \leq x_M$, and a time interval $0 \leq t \leq T$ are written in vector-form as the following coupled system of nonlinear conservation laws:

$$\partial_t \mathbf{u}(x, t) + \partial_x \mathbf{F}(\mathbf{u}(x, t)) = \mathbf{0}, \quad x_1 < x < x_M, t > 0, \quad (4a)$$

$$\mathbf{u}(x, 0) = \mathbf{u}_0(x), \quad x_1 \leq x \leq x_M, t = 0, \quad (4b)$$

where the 3-vector $\mathbf{u}(x, t)$ and *flux function* $\mathbf{F}(\mathbf{u}(x, t))$ are defined, respectively, as

$$\mathbf{u} = \begin{pmatrix} \rho \\ \rho u \\ E \end{pmatrix} \quad \text{and} \quad \mathbf{F}(\mathbf{u}) = \begin{pmatrix} \rho u \\ \rho u^2 + p \\ u(E + p) \end{pmatrix},$$

while the given initial data for the problem is

$$\mathbf{u}_0(x) = \begin{pmatrix} \rho_0(x) \\ (\rho u)_0(x) \\ E_0(x) \end{pmatrix}.$$

The *conservative variables* ρ , ρu , and E denote the *density*, *momentum*, and *energy* of a compressible gas, while the variable u represents the *velocity field*. The variable p denotes the *pressure function*, and according to the ideal gas law is given by

$$p = (\gamma - 1) \left(E - \frac{1}{2} \rho u^2 \right), \quad (5)$$

where γ is the adiabatic constant. Equations (4) represent the conservation of mass, linear momentum, and energy in the evolution of a compressible gas.

The total energy per unit volume E is the sum of kinetic energy and the potential energy,

$$E = \underbrace{\frac{1}{2} \rho u^2}_{\text{kinetic}} + \underbrace{\frac{p}{\gamma - 1}}_{\text{potential}}. \quad (6)$$

We also define the *specific internal energy per unit mass* of the system e , defined as

$$e = \frac{p}{(\gamma - 1)\rho}, \quad (7)$$

so that the total energy of the system may be written as the sum of the kinetic energy and the internal energy per unit volume ρe ,

$$E = \frac{1}{2} \rho u^2 + \rho e.$$

The gradient of the flux $\mathbf{F}(\mathbf{u})$ is given by

$$D\mathbf{F}(\mathbf{u}) = \begin{bmatrix} 0 & 1 & 0 \\ \frac{1}{2}(\gamma - 3)u^2 & (3 - \gamma)u & \gamma - 1 \\ -\gamma\frac{uE}{\rho} + (\gamma - 1)u^3 & \frac{\gamma E}{\rho} + \frac{3}{2}(1 - \gamma)u^2 & \gamma u \end{bmatrix}$$

with eigenvalues

$$\lambda_1 = u + c, \quad \lambda_2 = u, \quad \lambda_3 = u - c,$$

where $c = \sqrt{\gamma p/\rho}$ denotes the sound speed (see, for example, Toro [48]). These eigenvalues determine the wave speeds. Since the behavior of the various wave patterns is greatly influenced by the speed of propagation, we define the *maximum wave speed* $S(\mathbf{u})$ as

$$S(\mathbf{u}) = [S(\mathbf{u})](t) = \max_{i=1,2,3} \max_x \{|\lambda_i(x, t)|\}. \quad (9)$$

We are interested in solutions \mathbf{u} with discontinuous wave profiles, such as those with shock waves and contact discontinuities. The Rankine-Hugoniot (R-H) conditions determine the speed $\dot{\sigma} = \dot{\sigma}(t)$ of the moving shock or contact discontinuity, and represent conservation of mass, linear momentum and energy across the discontinuity (see, for example, [24]). For a shock wave, the R-H condition is given by the relation

$$F(\mathbf{u}_l) - F(\mathbf{u}_r) = \dot{\sigma}(\mathbf{u}_l - \mathbf{u}_r)$$

where the subscript l denotes the state to the left of the discontinuity, and the subscript r denotes the state to the right of the discontinuity. This means that the following three *jump conditions* must hold:

$$(\rho_l u_l) - (\rho_r u_r) = \dot{\sigma}(\rho_l - \rho_r) \quad (10a)$$

$$(\rho_l u_l^2 + p_l) - (\rho_r u_r^2 + p_r) = \dot{\sigma}((\rho u)_l - (\rho u)_r) \quad (10b)$$

$$(u_l(E_l + p_l)) - (u_r(E_r + p_r)) = \dot{\sigma}(E_l - E_r). \quad (10c)$$

Uniqueness for weak solutions that have jump discontinuities in general does not hold, unless entropy conditions are satisfied (see the discussion in §2.9.4 in [40]). However, solutions obtained in the limit of zero viscosity are known to satisfy the entropy condition and are hence unique. We refer the reader to [40] for a discussion of the convergence of C -method solutions as $\Delta x \rightarrow 0$.

2.2 A review of the original C -method

We now briefly review the C -method from [40], which is a spacetime smooth version of classical artificial viscosity with a *compression switch*:

$$\beta(\Delta x)^2 \partial_x \left(\mathbb{1}_{(-\infty, 0)}(\partial_x u) |\partial_x u| \partial_x u \right),$$

where the compression switch $\mathbb{1}_{(-\infty, 0)}(\partial_x u)$ ensures that artificial viscosity is only activated during compression, and not in regions of expansion where there are no shocks.

The localizing function $C(x, t)$ is given as the solution to the scalar reaction-diffusion equation¹

$$\partial_t C + \frac{S(\mathbf{u})}{\Delta x} C - S(\mathbf{u}) \Delta x \partial_{xx} C = \frac{S(\mathbf{u})}{\Delta x} G,$$

where the forcing G is

$$G \equiv G(x, t) = \mathbb{1}_{(-\infty, 0)}(\partial_x u) \frac{|\partial_x u|}{\max_x |\partial_x u|}, \quad (11)$$

and $S(\mathbf{u})$ is the maximum wave speed (9). The C -method artificial viscosity term is then given by

$$\tilde{\beta}(\Delta x)^2 \partial_x (C \partial_x u), \quad \text{where } \tilde{\beta} = \frac{\max_x |\partial_x u|}{\max_x C} \beta,$$

and the compressible Euler equations coupled with the C -method are written as the following Euler- C system:

$$\partial_t \rho + \partial_x(\rho u) = 0, \quad (12a)$$

$$\partial_t(\rho u) + \partial_x(\rho u^2 + p) = \tilde{\beta}(\Delta x)^2 \partial_x(\rho C \partial_x u), \quad (12b)$$

$$\partial_t E + \partial_x(u(E + p)) = \tilde{\beta}(\Delta x)^2 \partial_x(\rho C \partial_x(E/\rho)), \quad (12c)$$

$$\partial_t C + \frac{S(\mathbf{u})}{\Delta x} C - S(\mathbf{u}) \Delta x \partial_{xx} C = \frac{S(\mathbf{u})}{\Delta x} G(\partial_x u). \quad (12d)$$

Solutions of the Euler- C equations (12) converge to solutions of the Euler equations (4) as $\beta \rightarrow 0$ (see Section 2.9 in [40] for a proof). As was demonstrated in [40], a simple WENO-type numerical discretization of the Euler- C equations (12) (as will be described in §3) is an effective high-order scheme which compares favorably to the best state-of-the-art algorithms for the classical shock-tube experiments of Sod, Osher-Shu, Woodward-Colella, and LeBlanc. In particular, this simple WENO-type discretization of the C -method is able to remove the large overshoot in the LeBlanc contact discontinuity for the internal energy function (see [40]), whereas the other state-of-the-art schemes were not able to do so.

Herein, we generalize the C -method to allow for shock-wave wall collision and bounce-back, and introduce a wavelet-based *noise indicator* algorithm that locates high-frequency noise; a heat equation-based local solver will be used for noise removal. We shall also explain the well-known problem of wall-heating (see, for example, [43, 37]).

3 A new C -method for shock-wall collision

We now consider the highly singular problem of shock-wall collision and bounce-back, and specifically, the removal of spurious post collision oscillations.

¹We note that this scalar reaction-diffusion equation is not Galilean invariant. In the current implementation, the C -method is viewed purely as a numerical tool, whereas the function C may very well be viewed as an important physical quantity, in which case the C -equation itself should be preserved under Galilean transformations. This can be accomplished by the addition of an advection term to the current C -equation. We have checked for some 1- D examples that the addition of such a term has little effect on the demonstrated success of the C -method.

3.1 The Euler- C - W system

As a generalization to the Euler- C system (12), we consider the following coupled Euler- C - W system:

$$\partial_t \rho + \partial_x(\rho u) = 0, \quad (13a)$$

$$\partial_t(\rho u) + \partial_x(\rho u^2 + p) = \partial_x \left(\mathcal{B}^{(u)}(t) \rho C \partial_x u \right), \quad (13b)$$

$$\partial_t E + \partial_x(u(E + p)) = \partial_x \left(\mathcal{B}^{(E)}(t) \rho C \partial_x(E/\rho) \right), \quad (13c)$$

$$\partial_t C + \frac{S(\mathbf{u})}{\varepsilon \Delta x} C - \kappa \Delta x \cdot S(\mathbf{u}) \partial_{xx} C = \frac{S(\mathbf{u})}{\varepsilon \Delta x} G, \quad (13d)$$

$$\partial_t C_w + \frac{S(\mathbf{u})}{\varepsilon_w \Delta x} C_w - \kappa_w \Delta x \cdot S(\mathbf{u}) \partial_{xx} C_w = \frac{S(\mathbf{u})}{\varepsilon_w \Delta x} G, \quad (13e)$$

where

$$\mathcal{B}^{(u)}(t) = (\Delta x)^2 \cdot \frac{\max_x |\partial_x u|}{\max_x C} (\beta^u + \beta_w^u \cdot \bar{C}_w(t)), \quad (14a)$$

$$\mathcal{B}^{(E)}(t) = (\Delta x)^2 \cdot \frac{\max_x |\partial_x u|}{\max_x C} (\beta^E + \beta_w^E \cdot \bar{C}_w(t)), \quad (14b)$$

and where the smooth and localized bump function $\bar{C}_w(t)$ is defined as

$$\bar{C}_w(t) = \frac{C_w(x_M, t)}{\max_x C_w(x, t)}, \quad (15)$$

and x_M denotes the right boundary, where the shock-wall collision and bounce-back is assumed (for simplicity) to occur. Furthermore, $S(\mathbf{u})$ is the maximum wave-speed (9), and $G = G(x, t)$ is the forcing to the C -equation, defined by (11). The indicator function $\mathbb{1}_{(-\infty, 0)}(\partial_x u)$ is the *compression switch*, in which G is non-zero only if $\partial_x u < 0$. For convenience, we list all of the parameters and variables associated with the system (13) in Table 1. We note that due to the presence of the compression switch in the definition of G , we can instead define $G(x, t) = \mathbb{1}_{(-\infty, 0)}(\partial_x \rho) \cdot \frac{|\partial_x \rho|}{\max_x |\partial_x \rho|}$ and obtain identical results.²

We shall explain the use of this new $C_w(x, t)$ function and the localized time-function $\bar{C}_w(t)$ below, when we present the results of numerical experiments of shock-wall collision.

We remark that the artificial viscosity terms on the right-hand side of the momentum equation (13b) and the energy equation (13c) ensure that the total energy is conserved; in particular, the solution $E(x, t)$ of (13c) continues to obey the identity (6). For simplicity, we consider the case of periodic boundary conditions. On the one hand, integration of the energy equation (13c) over the spatial domain $[x_1, x_M]$ shows that $\frac{d}{dt} \int_{x_1}^{x_M} E dx = 0$. On the other hand, multiplying the momentum (13b) by u , integrating over the domain $[x_1, x_M]$, utilizing the conservation of mass (13a) together with the pressure identity (5), and the energy equation (13c), we find that

$$\frac{d}{dt} \int_{x_1}^{x_M} \left(\frac{1}{2} \rho u^2 + \frac{p}{\gamma - 1} \right) dx = 0.$$

²Indeed, this will be our strategy for the 2- D C -method that we introduce in [41].

This shows that the velocity u and pressure p adjust accordingly to maintain the relation (6), and that our modified Euler- C - W system conserves total energy.

Parameter / Variable	Description
β^u, β^E	artificial viscosity coefficients for the momentum and energy, respectively.
β_w^u, β_w^E	wall viscosity coefficients for the momentum and energy, respectively.
$S(\mathbf{u})(t)$	maximum wave speed $\max_x (\max \{ u(x, t) , u(x, t) \pm c \})$.
$\varepsilon, \varepsilon_w$	parameters controlling support of C and C_w , respectively.
κ, κ_w	parameters controlling smoothness of C and C_w , respectively.
$\overline{C}_w(t)$	smooth and localized bump function.

Table 1: Relevant parameters and variables for the Euler- C - W system (13).

3.2 Boundary conditions for the Euler- C - W system

We consider two types of boundary conditions on the interval $x_1 \leq x \leq x_M$. For many of the test problems, we employ the so-called *reflective* or *solid wall* boundary conditions at $x = x_1$ and $x = x_M$ and $t \geq 0$:

$$\partial_x \rho(x, t) = 0, \quad \rho u(x, t) = 0, \quad \partial_x E(x, t) = 0, \quad \partial_x C(x, t) = 0, \quad \partial_x C_w(x, t) = 0. \quad (16)$$

Alternatively, we shall sometimes use the *free flow* boundary conditions:

$$\partial_x \rho(x, t) = 0, \quad \partial_x (\rho u)(x, t) = 0, \quad \partial_x E(x, t) = 0, \quad \partial_x C(x, t) = 0, \quad \partial_x C_w(x, t) = 0. \quad (17)$$

3.3 The WENO- C - W algorithm

3.3.1 Discretization of the Euler- C - W system

We now describe the simple WENO-based space discretization scheme used for the Euler- C - W system (13). We use a formally fifth-order WENO reconstruction procedure together with upwinding, based on the sign of the velocity at the cell edges. We stress that the WENO-type discretization we use is highly simplified, and is not meant to be representative of the class of full WENO solvers. However, we note that, for certain problems, our simplified WENO-type discretization produces solutions with similar errors and convergence rates to those produced using a standard WENO scheme (see §5.2.5).

The spatial domain $x_1 \leq x \leq x_M$ is subdivided into M equally sized cells of width Δx , where the left-most and right-most cells are centered on the left and right boundaries, respectively. We denote the cell centers by x_i for $i = 1, \dots, M$, and the cell edges with the fractional index

$$x_{i+\frac{1}{2}} = \frac{x_i + x_{i+1}}{2}, \quad \text{for } i = 1, \dots, M - 1.$$

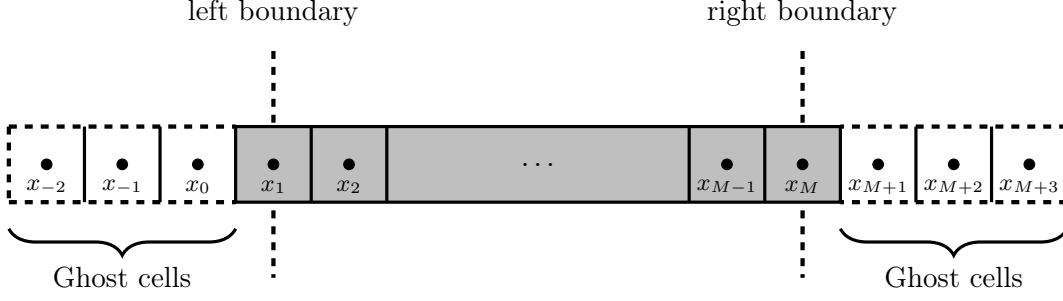


Figure 1: The grid, together with ghost cells, for the WENO- C - W algorithm.

Any quantity evaluated at a cell center x_i shall be denoted by w_i , and a quantity evaluated at a cell edge $x_{i+\frac{1}{2}}$ is denoted by $w_{i+\frac{1}{2}}$. Given a vector w_i corresponding to cell-center values, and vectors $z_{i-\frac{1}{2}}$ and $z_{i+\frac{1}{2}}$ corresponding to cell edge values, we define the j^{th} component by

$$\left[\text{WENO}(w_i, z_{i\pm\frac{1}{2}}) \right]_j = \frac{1}{\Delta x} \left(\tilde{w}_{j+\frac{1}{2}} z_{j+\frac{1}{2}} - \tilde{w}_{j-\frac{1}{2}} z_{j-\frac{1}{2}} \right),$$

where the cell-edge values $\tilde{w}_{j+\frac{1}{2}}$ are calculated using a standard fifth-order WENO reconstruction procedure (see [19], [47]) with upwinding based on the sign of $z_{j+\frac{1}{2}}$.

Then, defining the vectors $\mathbf{u} = [\rho, \rho u, E]^T$ and $\mathbf{C} = [C, C_w]^T$, we now construct the operators $\mathcal{A}_{\text{WENO}}$ and $\mathcal{B}_{\text{WENO}}$ as

$$[\mathcal{A}_{\text{WENO}}(\mathbf{u}_i, \mathbf{C}_i)] = \begin{bmatrix} \left[\text{WENO} \left(\rho_i, \hat{u}_{i\pm\frac{1}{2}} \right) \right]_i \\ \left[\text{WENO} \left((\rho u)_i, \hat{u}_{i\pm\frac{1}{2}} \right) \right]_i + \tilde{\partial}_4 p_i - \mathcal{B}^{(u)}(t) \cdot \frac{\tilde{\partial}_C(u_{i+\frac{1}{2}}) - \tilde{\partial}_C(u_{i-\frac{1}{2}})}{\Delta x} \\ \left[\text{WENO} \left((E+p)_i, \hat{u}_{i\pm\frac{1}{2}} \right) \right]_i - \mathcal{B}^{(E)}(t) \cdot \frac{\tilde{\partial}_C((E/\rho)_{i+\frac{1}{2}}) - \tilde{\partial}_C((E/\rho)_{i-\frac{1}{2}})}{\Delta x} \end{bmatrix} \quad (18)$$

and

$$[\mathcal{B}_{\text{WENO}}(\mathbf{u}_i, \mathbf{C}_i)] = \begin{bmatrix} \frac{S(\mathbf{u}_i)}{\varepsilon \Delta x} \{C_i - G_i\} + \frac{\tilde{\partial}_S C_{i+\frac{1}{2}} - \tilde{\partial}_S C_{i-\frac{1}{2}}}{\Delta x} \\ \frac{S(\mathbf{u}_i)}{\varepsilon_w \Delta x} \{[C_w]_i - G_i\} + \frac{\tilde{\partial}_S [C_w]_{i+\frac{1}{2}} - \tilde{\partial}_S [C_w]_{i-\frac{1}{2}}}{\Delta x} \end{bmatrix}. \quad (19)$$

Here, we have used the notation $\tilde{\partial}_4 p_i$ to denote the fourth-order central difference approximation for the derivative of the pressure at the cell center x_i :

$$\tilde{\partial}_4 p_i = \frac{p_{i-2} - 8p_{i-1} + 8p_{i+1} - p_{i+2}}{12 \cdot \Delta x}.$$

The cell-edge velocities $\hat{u}_{i\pm\frac{1}{2}}$ used for upwinding are calculated using a fourth-order averag-

ing:

$$\hat{u}_{i-\frac{1}{2}} = \frac{-u_{i-2} + 7u_{i-1} + 7u_i - u_{i+1}}{12}.$$

We have also used the notation $\tilde{\partial}_C(w_{i+\frac{1}{2}})$ and $\tilde{\partial}_S C_{i+\frac{1}{2}}$ to denote

$$\begin{aligned}\tilde{\partial}_C(w_{i+\frac{1}{2}}) &= \rho_{i+\frac{1}{2}} C_{i+\frac{1}{2}} \tilde{\partial} w_{i+\frac{1}{2}}, \\ \tilde{\partial}_S C_{i+\frac{1}{2}} &= \kappa \Delta x S(\mathbf{u}_i) \tilde{\partial} C_{i+\frac{1}{2}},\end{aligned}$$

respectively. Here, the notation $z_{i+\frac{1}{2}}$ denotes a quantity calculated at the cell edge $x_{i+\frac{1}{2}}$ using the standard averaging

$$z_{i+\frac{1}{2}} = \frac{z_i + z_{i+1}}{2},$$

while the quantity $\tilde{\partial} w_{i+\frac{1}{2}}$ denotes the central difference approximation for $\partial_x w$ at the cell edge $x_{i+\frac{1}{2}}$,

$$\tilde{\partial} w_{i+\frac{1}{2}} = \frac{w_{i+1} - w_i}{\Delta x}.$$

Now, given \mathbf{u}^n at a time $t = t_n = n\Delta t$, we evolve the solution as follows:

$$\mathbf{u}_i^{n+1} = \text{RK}(\mathbf{u}_i^n, \mathcal{A}_{\text{WENO}}(\mathbf{u}_i^n, \mathbf{C}_i^n)), \quad (20a)$$

$$\mathbf{C}_i^{n+1} = \text{RK}(\mathbf{C}_i^n, \mathcal{B}_{\text{WENO}}(\mathbf{u}_i^n, \mathbf{C}_i^n)), \quad (20b)$$

where RK denotes the explicit fourth-order Runge-Kutta time-integration method.

3.3.2 Discretization of boundary conditions and ghost node values

Boundary conditions for the functions C and C_w are imposed through the assigning of the so-called *ghost node* values. More precisely, the ghost node values for the functions C and C_w are prescribed via an even extension:

$$C_{1-k} = C_{1+k} \quad \text{and} \quad C_{M+k} = C_{M-k}, \quad (21)$$

for $k = 1, \dots, M_g$, where M_g is the number of ghost nodes. For our (formally) fifth-order WENO scheme, $M_g = 3$.

The associated boundary conditions for the conservative variables are also imposed via the ghost node conditions. For the Dirichlet boundary condition, an odd extension is used, while for the Neumann boundary condition, an even extension is used. More precisely, suppose that we wish to impose the free-flow boundary conditions (17). This is done by choosing the ghost node values as

$$\rho_{1-k} = \rho_{1+k} \quad \text{and} \quad \rho_{M+k} = \rho_{M-k}, \quad (22a)$$

$$\rho u_{1-k} = \rho u_{1+k} \quad \text{and} \quad \rho u_{M+k} = \rho u_{M-k}, \quad (22b)$$

$$E_{1-k} = E_{1+k} \quad \text{and} \quad E_{M+k} = E_{M-k}, \quad (22c)$$

for $k = 1, \dots, M_g$.

The solid wall boundary conditions (16) are imposed by replacing the even extension of the momentum in (22) with the odd extension of the momentum:

$$\rho_{1-k} = \rho_{1+k} \quad \text{and} \quad \rho_{M+k} = \rho_{M-k}, \quad (23a)$$

$$\rho u_{1-k} = -\rho u_{1+k} \quad \text{and} \quad \rho u_{M+k} = -\rho u_{M-k}, \quad (23b)$$

$$E_{1-k} = E_{1+k} \quad \text{and} \quad E_{M+k} = E_{M-k}, \quad (23c)$$

for $k = 1, \dots, M_g$. Again, it is easy to verify that the density ρ and the energy E satisfy the homogenous Neumann boundary condition in (16). To verify that the momentum satisfies the homogenous Dirichlet boundary condition, we need to use the momentum equation in the semi-discrete form (20). Suppose that at time-step n , the velocity at the boundaries vanishes: $u_M^n = u_1^n = 0$. For simplicity, we restrict to the right boundary in cell x_M . The even extensions of ρ and C and the odd extension of u mean that the diffusion term on the right-hand side of the momentum equation vanishes since

$$\begin{aligned} \tilde{\partial}_C \left(u_{M+\frac{1}{2}} \right) &= \rho_{M+\frac{1}{2}} \cdot C_{M+\frac{1}{2}} \cdot \frac{(u_{M+1} - u_M)}{\Delta x} \\ &= \rho_{M-\frac{1}{2}} \cdot C_{M-\frac{1}{2}} \cdot \frac{(-u_{M-1} + u_M)}{\Delta x} = \tilde{\partial}_C \left(u_{M-\frac{1}{2}} \right). \end{aligned}$$

Moreover, since the pressure p is evenly extended, the derivative at the boundaries $\tilde{\partial}_4 p_M$ and $\tilde{\partial}_4 p_1$, also vanishes. One can also check that the derivative of the flux term at the boundary vanishes: $\left[\text{WENO} \left((\rho u)_i, \hat{u}_{i \pm \frac{1}{2}} \right) \right]_M = 0$. This means that $\partial_t(\rho u) = 0$ at the boundaries, so that momentum satisfies $\rho u = 0$ at the boundaries for $t \geq 0$, provided that the initial momentum vanishes on the boundaries.

3.4 Using WENO- C - W for the Sod shock-wall collision problem

The reflection of a shock wave from a fixed wall was first considered in [10] from a theoretical viewpoint (see also [1, 36]). Further investigations in [37, 12] were done primarily in the context of the wall-heating phenomenon (to be discussed below). The reflection of a shock-wave from a non-rigid boundary was considered in [33, 18], wherein an artificial viscosity method was utilized to stabilize the solution.

As a motivating example, we first consider the classical Sod shock tube experiment. This is a Riemann problem on the domain $0 \leq x \leq 1$, with initial data given by

$$\begin{bmatrix} \rho_0 \\ (\rho u)_0 \\ E_0 \end{bmatrix} = \begin{bmatrix} 1 \\ 0 \\ 2.5 \end{bmatrix} \mathbb{1}_{[0, \frac{1}{2})}(x) + \begin{bmatrix} 0.125 \\ 0 \\ 0.25 \end{bmatrix} \mathbb{1}_{[\frac{1}{2}, 1]}(x) \quad \text{and} \quad \gamma = 1.4, \quad (24)$$

where $\mathbb{1}_{[a,b)}(x)$ denotes the indicator function on the interval $a \leq x < b$. The solution consists of a rarefaction wave, a contact discontinuity, and a shock wave. The shock propagating to the right collides with the wall, modeled by the point $x = 1$, at time $t \approx 0.28$. In Fig.2(a), we show the success of the WENO- C method for this problem prior to the collision of the shock wave with the wall at $x = 1$; however, as shown in Fig.2(b), the WENO- C scheme (without

the addition of the wall function $\overline{C}_w(t)$ is not sufficient to remove spurious oscillations post shock collision in the case of small $\beta = 0.5$. On the other hand, by setting $\beta = 4.0$, the velocity is mostly free of post shock-wall collision oscillations at $t = 0.36$, at the expense of an overly diffused shock profile prior to shock-wall collision at $t = 0.2$. Moreover, for more difficult problems, such as the LeBlanc problem considered in §5.4, very precise choices of the artificial viscosity parameters are required to maintain stability and correct wave speeds. Consequently, it is difficult to choose β such that the solutions both pre and post shock-wall collision are accurate and noise-free. The use of the wall viscosity will provide a nice solution strategy.

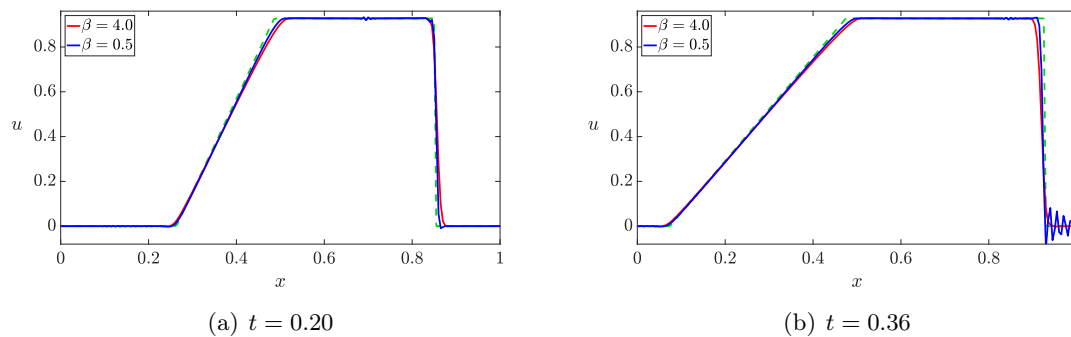


Figure 2: The velocity profile for the Sod shock tube problem, calculated using our WENO- C scheme with 201 cells. The blue and red curves are the velocity profiles and the dashed green curve is the exact solution.

3.4.1 An explanation of the temporal bump function $\overline{C}_w(t)$

We now explain the use of the new $C_w(x, t)$ function together with the temporal bump function $\overline{C}_w(t)$. We shall assume, for simplicity, that the shock wave is traveling to the right, so that the shock wave collides with the wall $x = 1$. Thanks to the homogeneous Neumann boundary condition $\partial_x C_w = 0$ at the wall $x = 1$, there is a smooth growth (in time) of the amplitude of $C_w(1, t)$ just prior to shock-wall collision, followed by a smooth decrease of amplitude during shock bounce-back.

In Fig.3, we illustrate the WENO- C - W scheme as applied to Sod. While the shock is away from the wall, $C_w(1, t)$ is zero, and thus by formula (15) so is $\overline{C}_w(t)$; see the purple curve in Fig.3(a). As the shock approaches the wall (as shown in Fig.3(b)), the Neumann boundary condition for the C_w -equation ensures that $\overline{C}_w(t)$ increases smoothly, until it reaches a maximum when the shock collides with the wall (Fig.3(c)), before smoothly decreasing back to zero as the shock moves away from the wall (Fig.3(d)).

In Fig.4, we plot the graph of $\overline{C}_w(t)$. The localized nature of the temporal bump function $\overline{C}_w(t)$ means that the extra viscosity, given by β_w in (14), is added only during shock-wall collision and bounce-back; prior to collision, no extra viscosity is added and the solution is consequently not overly diffused. In §5, we apply the WENO- C - W scheme to a number of different shock tube problems for shock collision and bounce-back.

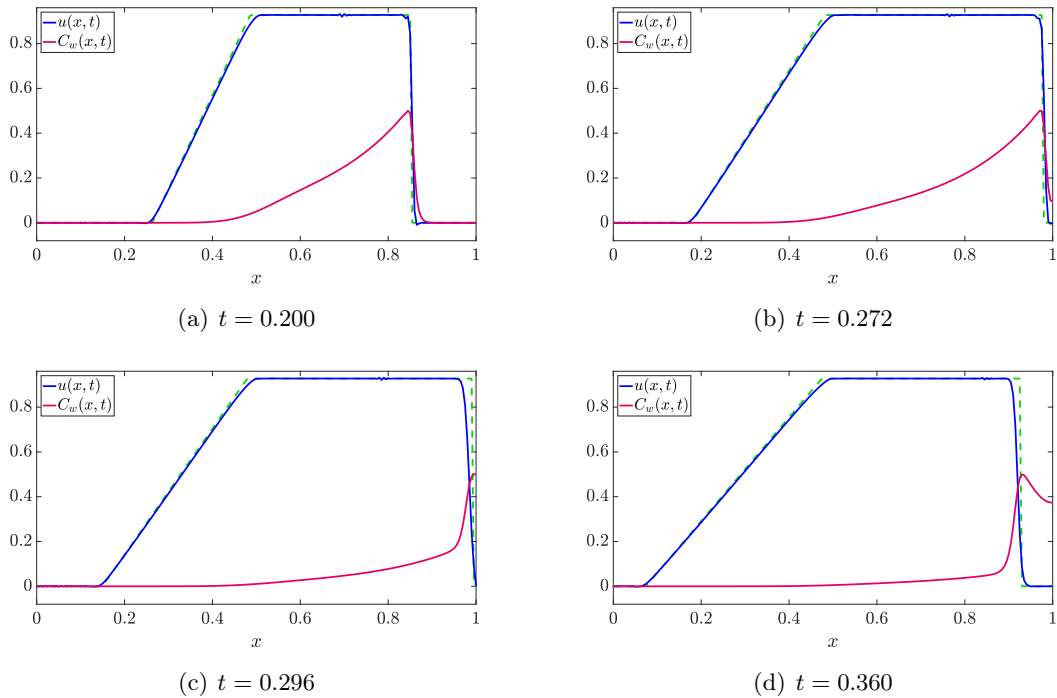


Figure 3: The velocity profile for the Sod shock tube problem, calculated using our WENO- C - W scheme with 201 cells. The blue curve is the velocity profile and the dashed green curve is the exact solution. The red curve is the (normalized and resized) function $C_w(x, t)$.

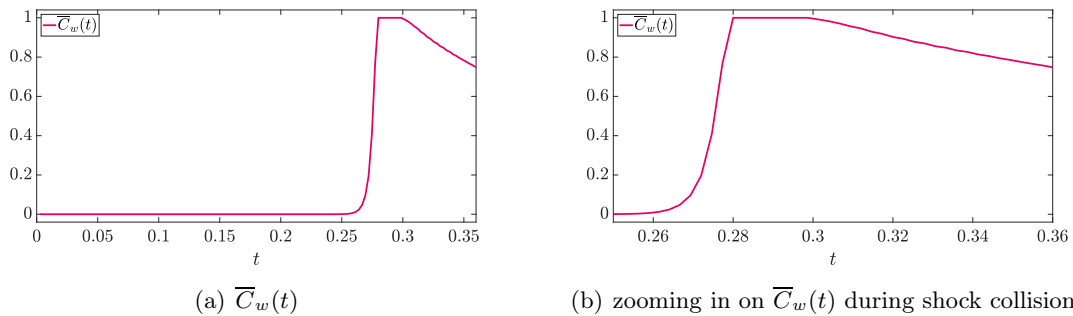


Figure 4: The wall indicator function $\bar{C}_w(t)$ for the Sod shock tube problem. The function is zero when the shock is away from the wall, increases smoothly as the shock approaches the wall, and reaches a maximum when the shock collides with the wall, before decreasing smoothly as the shock moves away from the wall.

3.4.2 A generalization of our algorithm to shock-shock collision problems

We remark here that a shock hitting a wall is simply a special case of shock-shock collision; indeed, the shock-wall collision problem may be viewed as the collision between two identical shocks but with different signs for the shock speed. A simple generalization of the Euler- C - W algorithm which allows for arbitrary shock-shock collision is obtained by redefining the

temporal bump function (15) with the new function

$$\overline{C}_w(t) = \sum_i \frac{C_w(x_i^*, t)}{\max_x C_w(x, t)}, \quad (25)$$

where $x_i^*(t)$ denotes the time-dependent local minima of the function $C_w(x, t)$ and approximates the location of the shock-shock collision (at the collision time). The functions $x_i^*(t)$ are analogous to the time-independent wall location x_M in the shock-wall collision problem (where the location of the collision is predetermined).

Fig.5 shows the density function during shock-shock collision. Also shown, is the temporal bump function \overline{C}_w , which naturally increases as two shock waves approach one another, and provides a natural method for the addition of spacetime smooth additional artificial viscosity during the shock-shock collision process. As can be seen, the two shocks collide at $t = 0.192$, at which time the function \overline{C}_w achieves its maximum value. We examine this problem of shock-shock collision in great detail in [42].

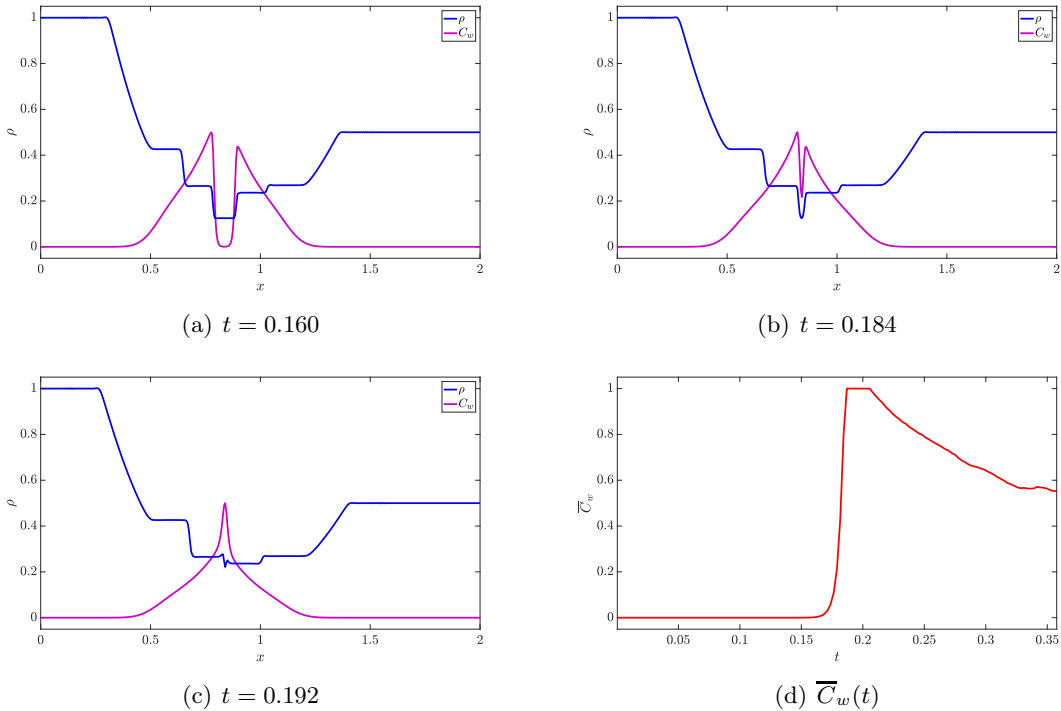


Figure 5: The density profile for a non-identical shock-shock collision problem. The blue curve is the density profile and the purple curve in Fig.5(a)-5(c) is the (normalized and resized) function $C_w(x, t)$. The red curve in Fig.5(d) is the temporal bump function $\overline{C}_w(t)$.

4 A wavelet-based noise indicator: the WENO- C - W - N method

Numerical solutions of gas dynamics often develop high-frequency noise. These (often small amplitude) spurious oscillations can occur if the time-step is too large or because of the

smearing of contact discontinuities. Large time-step noise can be seen with any explicit numerical scheme, while noise in the velocity field at the contact discontinuity is illustrated in Fig.6 for the Sod problem. This noise is caused by the slightly different slopes that the momentum and density profiles have at the contact discontinuity.

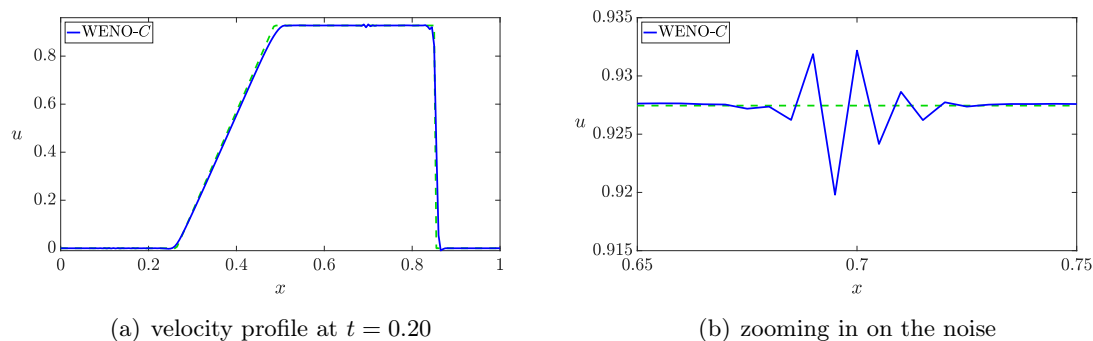


Figure 6: The velocity profile for the Sod shock tube problem, calculated using our WENO- C scheme with 201 cells. The blue curve is the velocity profile and the dashed green curve is the exact solution. There is noise in the region $x \in [0.65, 0.75]$. This is the location of the contact discontinuity in the density and momentum profiles.

To deal with the occurrence of spurious noise, we implement a localized *wavelet*-based noise indicator. Wavelets were first used in fluid dynamics in the analysis of turbulence by Farge [13] and Meneveau [34]. They have also been used in the numerical solution of PDE on adaptive grids (see the review paper [44]). With regards to noise detection and removal, wavelets have generally been used in the form of a nonlinear *filter*, in which a noisy function is first decomposed using wavelets, and the function is then *de-noised* by retaining only the low-frequency components. Such filtering techniques often over-smooth the noisy data, or introduce additional Gibbs-like oscillations [6].

The main novelty of our approach is the use of wavelets only for high-frequency noise detection, while noise removal is achieved by a highly localized heat equation approach.

4.1 Construction of wavelets

A wavelet is like a traditional wave (sine or cosine waves), but localized in space i.e. it has a finite support. We define a *mother wavelet* $\psi(x) = \psi_{0,0}(x)$ that represents the lowest frequency oscillation, and then use a dyadic scaling and integral translation to produce wavelets of higher frequencies:

$$\psi_{r,s}(x) = 2^{r/2}\psi(2^r x - s); \quad r = 0, 1, 2, \dots \quad \text{and} \quad s = \pm 1, \pm 3, \dots, \pm(2^r - 1).$$

Suppose that the spatial domain is given by $x_1 \leq x \leq x_M$. For our purposes, there are two key properties that the wavelet family $\{\psi_{r,s}\}$ needs to satisfy:

1. Zero mean:

$$\int_{x_1}^{x_M} \psi(x) dx = 0.$$

Note that due to the dyadic scaling and integral translation, this condition also ensures that wavelets of higher frequency have zero mean.

2. “Quasi-orthogonality” of the form:

$$\int_{x_1}^{x_M} \psi_{r,s}(x) \cdot \overline{\psi_{r,s'}(x)} dx = 0, \text{ for } r \geq 0 \text{ and } 0 \leq s, s' \leq 2^r - 1.$$

That is, each wavelet is orthogonal to every other wavelet of the same frequency. This is to ensure that one can locate exactly where each frequency is active.

We define our wavelets to take the form shown in Fig.7. Since we are only interested in the highest frequency noise, we provide the exact formula for the highest frequency wavelet as

$$\psi_i(x) = \begin{cases} -\frac{a}{\Delta x}(x - x_{2i-1}), & \text{if } x_{2i-1} \leq x \leq x_{2i-\frac{1}{2}} \\ +\frac{3a}{\Delta x}(x - x_{2i}) + a, & \text{if } x_{2i-\frac{1}{2}} \leq x \leq x_{2i} \\ -\frac{3a}{\Delta x}(x - x_{2i}) + a, & \text{if } x_{2i} \leq x \leq x_{2i+\frac{1}{2}} \\ +\frac{a}{\Delta x}(x - x_{2i+1}), & \text{if } x_{2i+\frac{1}{2}} \leq x \leq x_{2i+1} \end{cases} \quad (26)$$

for each $i = 1, 2, \dots, \frac{M-1}{2}$, where the notation $x_{k+\frac{1}{2}}$ denotes the midpoint of x_k and x_{k+1} . It is clear from formula (26) that each ψ_i is supported in the interval $\mathcal{I}_i := [x_{2i-1}, x_{2i+1}]$.

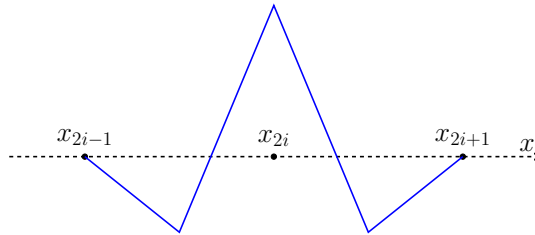


Figure 7: The highest frequency wavelet ψ_i .

The constant $a := \sqrt{3/\Delta x}$ in (26) is a normalization factor to ensure that the wavelets have L^2 norm equal to 1. Since the highest frequency wavelets have disjoint supports, it is obvious that the quasi-orthogonality property is satisfied. One can also check that the zero mean property is satisfied.

4.2 High-frequency noise detection

Given a discretized spatial domain, the highest frequency wavelet is supported over two grid cells and is shown in Fig.7. There are $\frac{M-1}{2}$ two-cell intervals in the computational domain. Each two-cell interval is denoted by \mathcal{I}_j , and there is a highest frequency wavelet $\psi_j(x)$ corresponding to each \mathcal{I}_j for every $j = 1, \dots, \frac{M-1}{2}$.

For a given function $f(x)$, we next compute the *wavelet coefficients* $\mathcal{C}_j(f)$ for this function. For each $j = 1, \dots, \frac{M-1}{2}$,

$$\mathcal{C}_j(f) := \langle f, \psi_j \rangle_{L^2} = \int_{\mathcal{I}_j} f(x) \psi_j(x) dx \text{ for } j = 1, \dots, \frac{M-1}{2}.$$

Given the cell-center values $f(x_{2j-1}), f(x_{2j}), f(x_{2j+1})$, we can approximate the given function $f(x)$ on the interval $\mathcal{I}_j = [x_{2j-1}, x_{2j+1}]$ by a piecewise linear function $\tilde{f}(x)$; in particular, we define $\tilde{f}(x)$ by linear interpolation of the cell-center values of $f(x)$. We then approximate the wavelet coefficients by $\mathcal{C}_j(f) \approx \mathcal{C}_j(\tilde{f})$, and can compute

$$\mathcal{C}_j(\tilde{f}) = \langle \tilde{f}, \psi_j \rangle_{L^2} = -\sqrt{\frac{\Delta x}{48}} \cdot [f(x_{2j+1}) - 2f(x_{2j}) + f(x_{2j-1})]. \quad (27)$$

Notice that the right-hand side of (27) is proportional to the second-order central difference approximation to $f''(x_{2i})$. Also, note that if $f(x_{2i}) = \frac{1}{2}(f(x_{2i+1}) + f(x_{2i-1}))$, i.e., if the function \tilde{f} is linear on \mathcal{I}_i , then the associated wavelet coefficient is zero. This is crucial in ensuring that only the *highest* frequency noise is detected.

The magnitude of the wavelet coefficients grows with the amplitude of the high-frequency oscillations. For example, consider the case that $f(x)$ is a hat function over the interval $\mathcal{I}_j = [x_{2j-1}, x_{2j+1}]$ and that $f(x_{2j-1j}) = f(x_{2j+1}) = 0$. Then the amplitude of the oscillation is given by the magnitude at the peak of the hat, $f(x_{2j})$, and $|\mathcal{C}_j(f)|$ is proportional to $f(x_{2j})$. Consequently, $|\mathcal{C}_j(f)|$ grows linearly with the amplitude of the oscillation.

On the other hand, suppose that we have a lower frequency oscillation, given by a hat function that spans 4 cells, say the intervals \mathcal{I}_j and \mathcal{I}_{j+1} . In each of these intervals, the oscillating function is linear, so that the associated wavelet coefficients $\mathcal{C}_j(f)$ and $\mathcal{C}_{j+1}(f)$ are equal to zero. This illustrates the fact that the highest frequency wavelets detect *only* the highest frequency noise.

4.3 Noise detection in the presence of a shock wave

We next examine the noise detection algorithm, applied to a function $u(x)$ which has a shock discontinuity. For $j = 1, \dots, (M-1)/2$, we again compute the wavelet coefficients $\mathcal{C}_j(u)$ for each two-cell interval \mathcal{I}_j according to (27). Suppose the shock discontinuity occurs spans the two-cell interval \mathcal{I}_j ; then, on \mathcal{I}_j the shock curve is essentially linear and $\mathcal{C}_j(u) = 0$, but if the shock is out of phase by one cell with \mathcal{I}_j , then the wavelet coefficient $\mathcal{C}_j(u)$ can be large (see Fig.8).

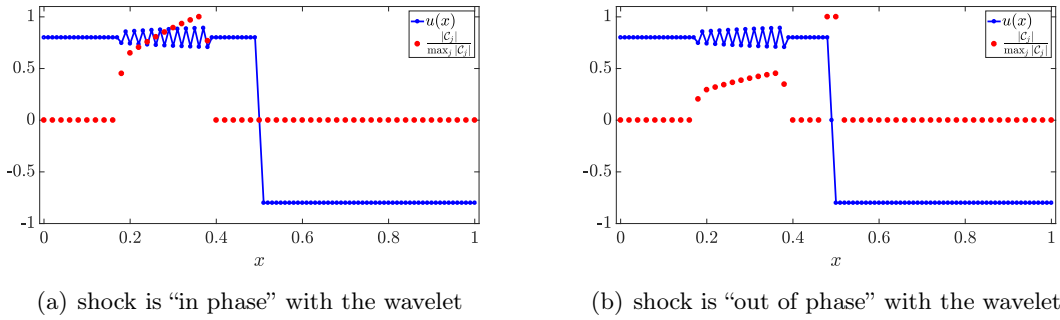


Figure 8: Wavelet coefficients at the shock curve compared with wavelet coefficients in regions where there is noise. The blue curve is $u(x)$, and the red dots indicate the relative magnitude of the associated wavelet coefficient $\mathcal{C}_j(u)$. The wave profile in Fig.8(b) is identical to that in Fig.8(a), but shifted by one cell to the left.

In order to avoid over-diffusion at the shock, we prevent noise detection near shock discontinuities. This is achieved by noting that the function $C(x, t)$ attains a local maximum for points x along the shock curve. Consequently, we locate the local maximums of $C(x, t)$, by finding the cells for which $\partial_x C = 0$ and $\partial_{xx} C < 0$. We then deactivate the noise detection in the cells surrounding the shock curve.

Having deactivated the noise indicator near the discontinuity, the largest wavelet coefficients are now those where the high-frequency oscillations exist. We may then define the *noise detector function* $\mathbb{1}_{\text{noise}}(x)$ as follows: for each $j = 1, \dots, \frac{M-1}{2}$ and $x \in \mathcal{I}_j$, we set $\mathbb{1}_{\text{noise}}(x) = 1$ if $|\mathcal{C}_j(u)| > \mathcal{C}_{\text{ref}} > 0$ and set $\mathbb{1}_{\text{noise}}(x) = 0$ otherwise.

The constant \mathcal{C}_{ref} is obtained by computing the wavelet coefficient of a standard hat function on the interval $[-\Delta x, +\Delta x]$ with amplitude δh :

$$\mathcal{C}_{\text{ref}} = \delta h \cdot \sqrt{\frac{\Delta x}{12}}. \quad (28)$$

4.4 Noise removal algorithm

Having described the noise detection algorithm, we next propose an efficient scheme for removing noise from a given function $u(x)$ by solving a localized heat equation over the collection of intervals \mathcal{I}_j where high-frequency noise has been detected.

The union of all noisy intervals \mathcal{I}_j consists of K connected intervals V_1, \dots, V_K . For each set V_k , $k = 1, \dots, K$, we define the set W_k by affixing one cell on the left and one cell on the right. We then solve a localized heat equation for the “de-noised” solution $w(x, \tau)$ in each of the domains W_k :

$$\partial_\tau w(x, \tau) = \eta \cdot \partial_{xx} w(x, \tau), \quad \text{for } x \in W_k \text{ and } \tau \geq 0, \quad (29a)$$

$$w(x, 0) = u(x), \quad \text{for } x \in W_k, \quad (29b)$$

$$w(x, \tau) = u(x), \quad \text{for } x \in \partial W_k, \quad (29c)$$

where $0 < \eta \ll 1$ is a small constant, which we refer to as the noise removal viscosity. The function $w(x, \tau) = u(x)$ for $x \in \left(\bigcup_{k=1}^K W_k\right)^c$ and $\tau \geq 0$. We remark that the time τ

is a “fictitious” time, introduced for the diffusion mechanism. Equation (29b) is the initial condition over the intervals where noise has been detected, and (29c) is a Dirichlet boundary condition ensuring that $w(x, \tau)$ continuously transitions to $u(x)$.

We use an explicit scheme to solve (29), and in practice, one time-step is sufficient to remove noise. If an explicit time-stepping scheme is used to solve (29), it is not necessary to construct the domains W_k . Instead, one can simply use the noise indicator function $\mathbb{1}_{\text{noise}}(x)$, and solve a modified heat equation:

$$\partial_\tau w(x, \tau) = \eta \cdot \mathbb{1}_{\text{noise}}(x) \cdot \partial_{xx} w(x, \tau), \quad \text{for } x_1 < x < x_M \text{ and } \tau \geq 0, \quad (30a)$$

$$w(x, 0) = u(x), \quad \text{for } x_1 < x < x_M, \quad (30b)$$

$$w(x, \tau) = u(x), \quad \text{for } x = x_1 \text{ and } x = x_M. \quad (30c)$$

The utilization of an explicit scheme results in the stability constraint $\eta \Delta \tau / (\Delta x)^2 < 1/2$. However, in practice, we have found that much smaller values $\eta \Delta \tau / (\Delta x)^2 \ll 1/2$ are sufficient to dampen spurious noise. We also remark that the use of a single time-step means that the noise removal provided by the localized heat equation can be viewed as a *filtering* process, in which noise is removed through a local averaging. Consequently, the averaging provided by the Laplacian term on the right-hand side of (30a), namely $(w_{i+1} - 2w_i + w_{i-1})/2$, can be replaced by other local averages, such as that provided by Gaussian filtering [3].

However, we wish to stress that there is a distinction between the operation of *smoothing* a noisy function and the noise removal process we have outlined. While, of course, removing high-frequency noise does indeed smooth the function, because we remove highly localized (in space and time) packets of oscillations, the procedure is quite different to more traditional smoothing algorithms, in which one uses truncation of frequencies in Fourier space or the analogous hyperviscosity operators in physical space. As such, it is difficult to obtain analytically the truncation error by means of a Taylor expansion, but it is possible to measure the error improvement by virtue of convergence studies comparing the algorithm with and without the noise removal algorithm activated. We provide results of such studies in §5.

4.5 The WENO- C - W - N algorithm

We now describe how we implement the above noise indicator algorithm for the Euler equations. The algorithm proceeds in two stages; in the first stage, we use the WENO- C - W scheme described in §3.3 to solve for an intermediary solution $\tilde{\mathbf{u}} = [\tilde{\rho}, \tilde{\rho}u, \tilde{E}]^T$; in the second stage, we feed this intermediary solution $\tilde{\mathbf{u}}$ into the noise indicator algorithm to de-noise the solution. The two-stage process is now described.

1. An intermediary solution $\tilde{\mathbf{u}}$ is obtained as

$$\begin{aligned} \tilde{\mathbf{u}}_i &= \text{RK}(\mathbf{u}_i^n, \mathcal{A}_{\text{WENO}}(\mathbf{u}_i^n, \mathbf{C}_i^n)), \\ \mathbf{C}_i^{n+1} &= \text{RK}(\mathbf{C}_i^n, \mathcal{B}_{\text{WENO}}(\mathbf{u}_i^n, \mathbf{C}_i^n)). \end{aligned}$$

2. The intermediate velocity \tilde{u}_i is then de-noised using the procedure described in §4.3 and §4.4, producing the noise-free velocity $u(x, t_{n+1})$. The updated solution $\mathbf{u}(x, t_{n+1})$

is then obtained as

$$\mathbf{u}(x, t_{n+1}) \equiv (\rho(x, t_{n+1}), \rho u(x, t_{n+1}), E(x, t_{n+1})) := \left(\tilde{\rho}(x), \tilde{\rho}(x) \cdot u(x, t_{n+1}), \tilde{E}(x) \right).$$

REMARK 1. Implementation of our noise removal scheme has been motivated by the high-frequency oscillations of the velocity field that occur exactly at the contact discontinuity (see, for example, Fig.6). We note that once the noise indicator function $\mathbb{1}_{\text{noise}}(x)$ is computed, there are many possible choices for the noise removal portion of the algorithm. For example, while our implemented algorithm only removes high-frequency oscillations from the velocity, we could also remove such oscillations from ρ and E , and we could in place of the velocity field, instead remove oscillations from the momentum ρu . We have found that any of these choices produce the same relative errors in the one-dimensional test problems considered herein. Moreover, as we demonstrate in §5, the removal of high-frequency oscillations from u alone, is sufficient to remove noise from the density and energy as well. A more detailed examination of various noise removal algorithms (as well as those more ideally suited for parallelization) is made in [42].

5 Numerical simulations of classical shock tube experiments

In this section, we show results of the discretized C -method for a variety of classical shock tube experiments. For some of the problems, we will compare against WENO-based classical artificial viscosity schemes and Noh schemes. See Appendix A and Table 12 for a description of all of the numerical methods employed herein.

Parameter / Variable	Description
β^u, β^E	artificial viscosity coefficients for the momentum and energy, respectively.
β_w^u, β_w^E	wall viscosity coefficients for the momentum and energy, respectively.
$\delta h, \eta$	amplitude of noise and noise removal viscosity, respectively.
$\varepsilon, \varepsilon_w$	parameters controlling support of C and C_w , respectively.
κ, κ_w	parameters controlling smoothness of C and C_w , respectively.

Table 2: Relevant parameters and variables used in the numerical tests.

As with any artificial viscosity scheme, parameters must be chosen for the problem under consideration. Before presenting our numerical results, we consider this issue for the C -method, whose parameters are listed in Table 2. The artificial viscosity parameters β are chosen in the following manner: we set $\beta^E = 0$, choose β^u, β_w^u large enough so that post-shock oscillations are removed both pre and post shock-wall collision, then choose β_w^E

large enough so that the wall-heating phenomenon (discussed later in §5.2) does not occur. A similar philosophy is applied to choice of parameters for the noise detection and removal algorithm: first, we determine the amplitude of highest-frequency oscillation δh and then choose the artificial viscosity parameter η large enough to diffuse the noise.

The parameters ε , ε_w , κ , and κ_w are $O(1)$ constants. Setting a larger value for ε or ε_w serves to increase the support of the corresponding C -function, while increasing the value of κ or κ_w produces smoother C -functions. For certain problems, smoothing the C -variables by using a larger κ further minimizes noise that occurs in the solution.

In Appendix C we demonstrate the accuracy of the C -method when the values of the parameters ε , ε_w , κ , and κ_w are fixed values for the different test problems. It is shown that the differences between the solutions computed using the optimized parameter sets we use for the problems in this section and the fixed-parameter sets we use for the runs in Appendix C are minimal, and that the fixed choice of parameters can be used for general problems. However, we wish to emphasize that one of the strengths of the C -method is its flexibility to optimize parameters for specific features associated with particular data.

The error analysis and convergence studies we perform for the numerical experiments considered in the following sections use the L^1 , L^2 , and L^∞ norms. Given two functions $f(x)$ and $g(x)$ defined on the computational grid with M cells, these error norms are defined by

$$\|f - g\|_{L^1} = \frac{1}{M} \sum_{i=1}^M |f(x_i) - g(x_i)|, \quad (31a)$$

$$\|f - g\|_{L^2} = \sqrt{\frac{1}{M} \sum_{i=1}^M |f(x_i) - g(x_i)|^2}, \quad (31b)$$

$$\|f - g\|_{L^\infty} = \max_{i=1, \dots, M} |f(x_i) - g(x_i)|. \quad (31c)$$

As stated by Greenough & Rider [15], the L^1 and L^2 norms provide a global view of the errors in the computed solution, whereas the L^∞ norm highlights local errors, such as the under-shoot or overshoot that occurs at a discontinuity. Thus, these three norms together provide a precise *quantitative* description of the errors of numerical solutions, and complement the *qualitative* evidence we provide through the visualization of numerical simulations.

5.1 Linear advection

We begin by considering a linear advection problem to demonstrate the high-order convergence of the base WENO scheme. The domain is $0 \leq x \leq 1$, the adiabatic constant is $\gamma = 1.4$, the initial data is

$$\begin{bmatrix} \rho_0 \\ (\rho u)_0 \\ E_0 \end{bmatrix} = \begin{bmatrix} 1 + 0.5 \sin(2\pi x) \\ 1 + 0.5 \sin(2\pi x) \\ 0.5 + 0.25 \sin(2\pi x) + \frac{1}{\gamma-1} \end{bmatrix},$$

and we employ periodic boundary conditions. In the exact solution, the velocity and pressure remain a constant value of 1, while the initial density field is advected by the velocity, so

that the density at time t satisfies $\rho(x, t) = \rho_0(x - t)$. We employ our simplified WENO scheme on grids with 51, 101, 201, and 401 cells. Each simulation is run with a CFL number of approximately 0.6, and the final time is $t = 1.0$.

In Table 3, we list the L^1 error of the computed density minus the exact solution; as expected, the solutions converge with almost fifth-order accuracy.

Scheme		Cells			
		51	101	201	401
WENO	Error	7.298×10^{-6}	2.318×10^{-7}	7.526×10^{-9}	2.654×10^{-10}
	Order	–	4.977	4.945	4.826

Table 3: L^1 error of the computed density minus the exact solution and convergence for the linear advection problem.

5.2 The Sod shock tube problem

The data for the Sod shock tube is given in (24), with the exact solution given by a shock wave, a rarefaction wave, and a contact discontinuity. To simulate the shock-wave wall collision, we employ reflective boundary conditions (16). In the tests below, we employ our WENO- C - W scheme with 201 cells.

5.2.1 The wall-heating problem in the Sod shock tube

We first demonstrate the well-known wall-heating problem ([37, 43]) in which an anomalous slope appears in the density and internal energy upon shock bounce-back. We shall then explain what the root cause of this problem is, and its solution.

We begin by choosing the parameters in equations (13) and (14) as

$$\begin{aligned} \beta^u &= 0.5, & \beta^E &= 0.0, & \beta_w^u &= 3.0, & \beta_w^E &= 0.0 \\ \varepsilon &= 1.0, & \kappa &= 5.0, & \varepsilon_w &= 50.0, & \kappa_w &= 1.0. \end{aligned}$$

The resulting solutions for the velocity before and after the shock-wall collision are shown in Fig.9. Before the shock collision with the wall (Fig.9(a)), the solution maintains a sharp shock front. After the shock collision (Fig.9(b)), the high-frequency oscillations behind the shock wave are damped-out for sufficiently large $\beta_w^u > 0$, while maintaining a sharp front.

While post-collision oscillations in the density profile are suppressed, Fig.10 shows the presence of the anomalous density slope $\partial_x \rho(1, t)$ at the wall (which should be zero). This incorrect slope is termed *wall heating* because the undershoot in the density results in an overshoot in the internal energy (7) (and hence temperature) at the wall. Noh [37] suggested that wall heating would occur in *any* artificial viscosity scheme, and is in fact built into the exact solutions of the difference equations of the artificial viscosity method. Menikoff [35] argues that wall-heating is caused by the *smearing* of the shock curve that occurs with any artificial viscosity scheme, and is thus unavoidable. Rider [43] argues that incorrect wave speeds result in too much or too little dissipation.

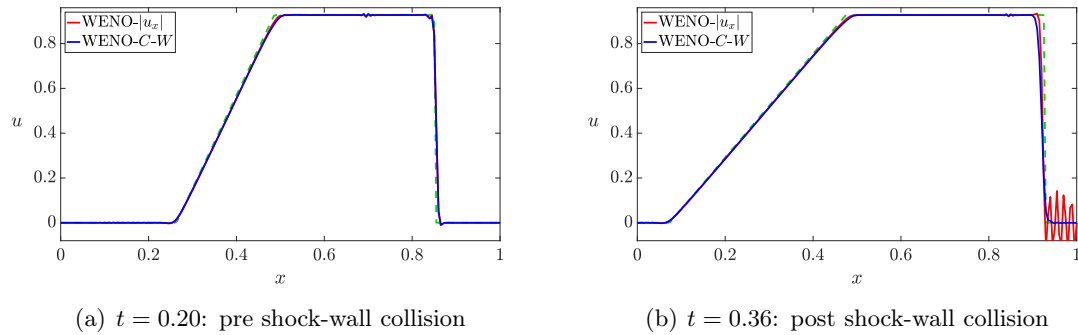


Figure 9: The velocity profile for the Sod shock tube problem, with the wall viscosity activated for the momentum equation. The dashed green curve is the exact solution.

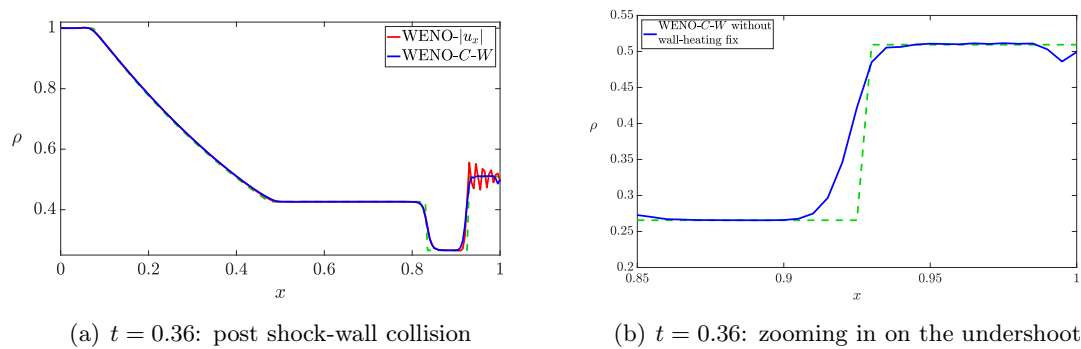


Figure 10: The density profile for the Sod shock tube problem, calculated with the wall viscosity activated for the momentum equation. The dashed green curve is the exact solution.

In fact, it appears that the wall-heating error is the result of the misalignment of the *gradient of fluxes* for the density, momentum and energy equations, which in turn is caused by a slight difference in the speed of the shock fronts for the density, momentum and energy. We define the *forcing terms*

$$\begin{aligned}\mathcal{H}(\rho) &= -\partial_x(\rho u), \\ \mathcal{H}(\rho u) &= -\partial_x(\rho u^2 + p) + \partial_x\left(\mathcal{B}^{(u)}(t) \rho C \partial_x u\right), \\ \mathcal{H}(E) &= -\partial_x(u(E + p)) + \partial_x\left(\mathcal{B}^{(E)}(t) \rho C \partial_x(E/\rho)\right).\end{aligned}$$

In Fig.11, we compare the energy and density profiles, along with the terms $\mathcal{H}(\rho)$, $\mathcal{H}(\rho u)$, and $\mathcal{H}(E)$, all suitably resized³ for ease of comparison, at various times just before or after the shock fronts have collided with the wall, zoomed-in on the region next to the wall. In Fig.11(a), the density and energy profiles are very similar, but the forcing terms are slightly

³More precisely, we plot the following: first, $\frac{3}{2} \frac{\mathcal{H}}{\max_{\Omega} \mathcal{H}}$ for each of the forcing terms $\mathcal{H}(\rho)$, $\mathcal{H}(\rho u)$, and $\mathcal{H}(E)$; second, the function $1.1928 + 4.4403\rho$; and finally, the energy E .

misaligned; it is clear that $\mathcal{H}(E)$ is slightly behind both $\mathcal{H}(\rho)$ and $\mathcal{H}(\rho u)$. This misalignment causes the solution profiles for the energy and density to begin to diverge, as can be seen in Fig.11(b). Again, there is a misalignment between the forcing terms $\mathcal{H}(E)$ and $\mathcal{H}(\rho)$. As the shock moves away from the wall in Fig.11(c) and Fig.11(d), the difference between the solution profiles is now clear. Even though the forcing terms are now better aligned, the earlier misalignment ensures that the difference between the energy and density profiles is permanent.

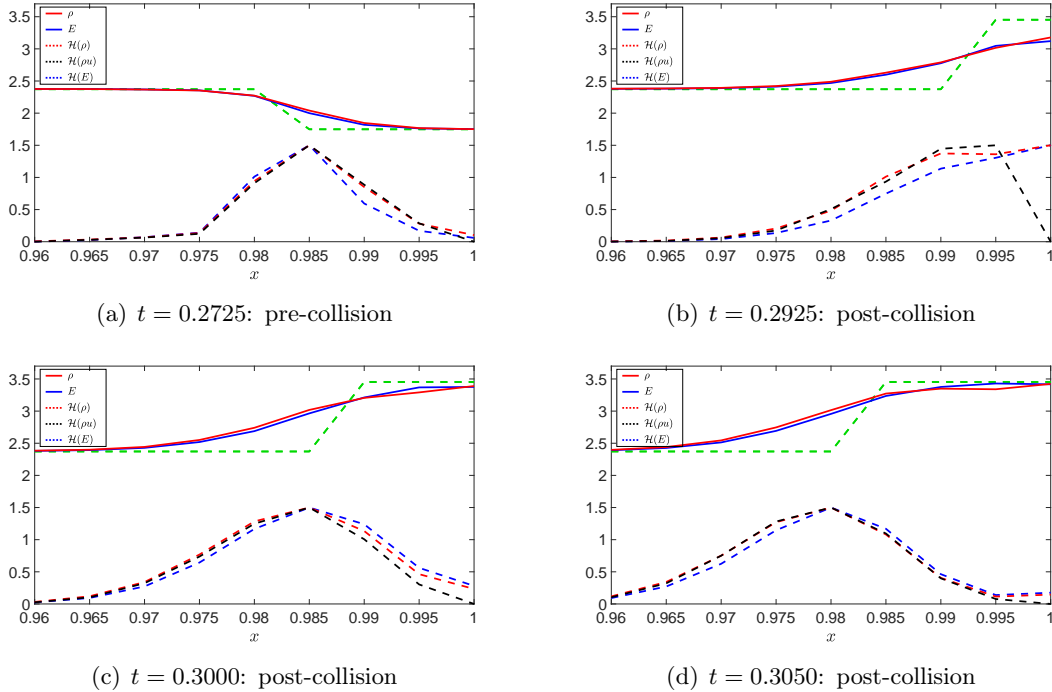


Figure 11: Comparison of the energy and energy forcing term $\mathcal{H}(E)$ (blue/blue dashed) with the density, suitably resized, and the density forcing term $\mathcal{H}(\rho)$ (red/red dashed) and the momentum forcing term $\mathcal{H}(\rho u)$ (black dashed) for the Sod shock tube problem with the wall viscosity activated for the momentum equation. The green dashed curve is the exact solution. The figures shown are zoomed in at the shock just before or just after the shock front has collided with the wall at $x = 1$.

5.2.2 A solution to the wall-heating problem

The solution to the wall heating problem suggested by Noh [37] is the addition of a heat conduction term to the energy equation. For the WENO-Noh scheme we implement in this study, we shall use a heat conduction term of the form⁴

$$\partial_x \left(\beta_{\text{Noh}}^E \rho |\partial_x u| \partial_x e \right), \quad (32)$$

⁴In equations (2.1)-(2.5) in the paper of Noh [37], there is, in fact, an additional term proportional to $-\rho |\partial_x u|^2 \partial_x u$ on the right-hand side of (32). We have found that this term is not necessary to remove the wall-heating error, and thus omit it from the Noh scheme we implement in this paper.

where $e = p/(\gamma - 1)\rho = c_v\Theta$ is the internal energy of the system, proportional to the temperature Θ , with c_v the specific heat capacity at a constant volume.

We use the following artificial (wall) viscosity for the energy equation (13c):

$$\partial_x \left(\mathcal{B}^{(E)}(t) \rho C \partial_x (E/\rho) \right). \quad (33)$$

There are two differences between the terms (33) and (32):

1. While (32) uses the oscillatory localizing coefficient $|\partial_x u(x, t)|$, we instead use the space-time smooth localizer $C(x, t)$.
2. We use $\partial_x (E/\rho)$ in our diffusion operator rather than the function $\partial_x e$. This difference can be explained as follows: equation (7) shows that

$$\partial_x \left(\mathcal{B}^{(E)}(t) \rho C \partial_x (E/\rho) \right) = \partial_x \left(\mathcal{B}^{(E)}(t) \rho C \partial_x e \right) + \partial_x \left(\mathcal{B}^{(E)}(t) \rho C u \partial_x u \right). \quad (34)$$

Hence, (34) has a similar form to (32) (with C replacing $|u_x|$), but with the additional term $\partial_x \left(\mathcal{B}^{(E)}(t) \rho C u \partial_x u \right)$. Indeed, the two terms in (34) are both proper diffusion operators near shock waves. This is easy to see: multiplying (34) by E and integrating by parts then shows that

$$\int_{x_1}^{x_M} \mathcal{B}^{(E)}(t) \rho C \partial_x e \partial_x E \, dx + \int_{x_1}^{x_M} \mathcal{B}^{(E)}(t) \rho C u \partial_x u \partial_x E \, dx.$$

At the shock, $\partial_x e$ has the same sign as $\partial_x E$ so that $\int_{x_1}^{x_M} \mathcal{B}^{(E)}(t) \rho C \partial_x e \partial_x E \, dx \geq 0$; moreover, in the case of a right-traveling shock front, $\partial_x u < 0$, $\partial_x E < 0$ and $u > 0$ at the shock, so that $\int_{x_1}^{x_M} \mathcal{B}^{(E)}(t) \rho C u \partial_x u \partial_x E \, dx \geq 0$, while for a left-moving shock, $\partial_x u < 0$, $\partial_x E > 0$ and $u < 0$, so that once again $\int_{x_1}^{x_M} \mathcal{B}^{(E)}(t) \rho C u \partial_x u \partial_x E \, dx \geq 0$. This then ensures that (33) is a *dissipative* operator and that the structure of the artificial viscosity term in (33) adjusts the Noh-type dissipation $\partial_x \left(\mathcal{B}^{(E)}(t) \rho C \partial_x e \right)$ by the velocity-dependent term $\partial_x \left(\mathcal{B}^{(E)}(t) \rho C u \partial_x u \right)$.

In our numerical experiments, presented below, we compare Noh's scheme, called WENO-Noh (see Appendix A), with our WENO- C - W scheme. For WENO-Noh, we set $\beta_{\text{Noh}}^u = 15.0$ and $\beta_{\text{Noh}}^E = 10.0$ in (40). These viscosity coefficients were chosen in the following manner: β_{Noh}^u was first chosen large enough to suppress the post-collision oscillations, and then β_{Noh}^E was chosen to correct the wall-heating error. In our WENO- C - W scheme, we set $\beta^u = 0.5$, $\beta_w^u = 3.0$, $\beta^E = 0.0$, and $\beta_w^E = 6.0$.

In Fig.12, we compare the velocity and density profiles computed with the two schemes above. It is clear that the WENO- C - W scheme produces a superior solution both before and after the shock-wall collision. The large amount of viscosity needed in the WENO-Noh scheme post-collision means that the solution prior to shock-wall collision is affected, with a smeared shock curve and overshoot at the top of the expansion wave. Moreover, even the relatively large value of β_{Noh}^u as compared with $\beta^u + \beta_w^u$ is unable to fully suppress the oscillations behind the shock curve that occur post-collision. This is due to the smoothness of the localizing coefficient C as compared with the rough nature of $|\partial_x u|$.

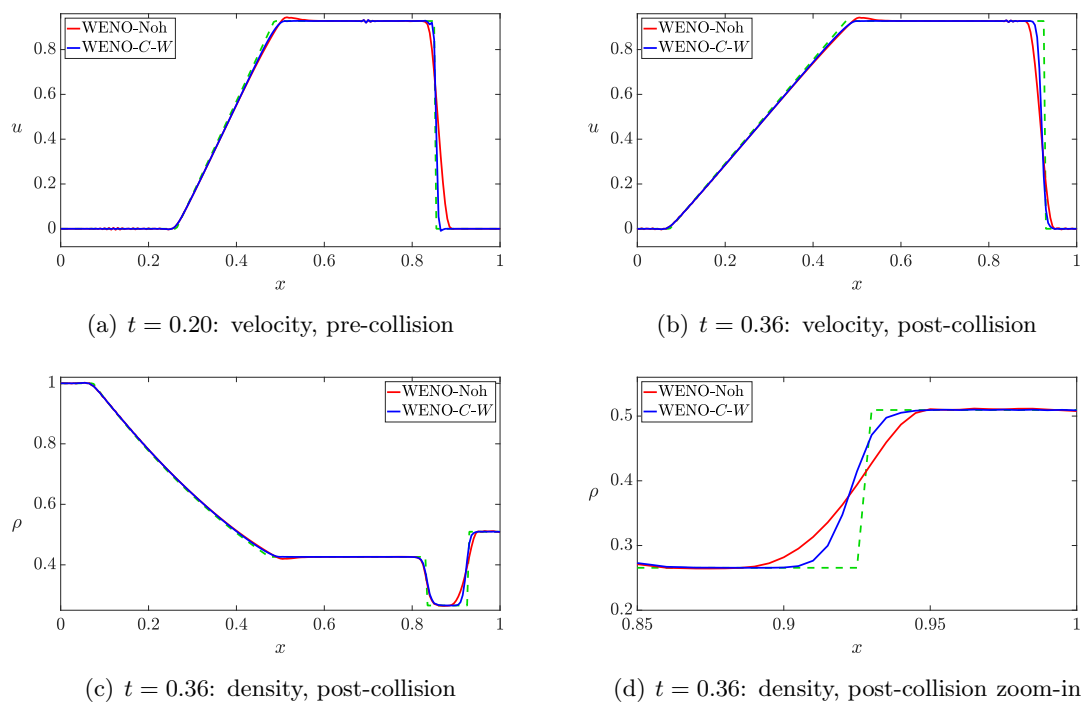


Figure 12: The velocity and density profiles for the Sod shock tube problem before and after shock-wall collision.

As is the case with the velocity profile, prior to shock collision the WENO- C - W scheme produces a superior solution for the density profile, with a much sharper shock front and more accurate expansion wave. Post-collision, the heat conduction terms ensure that neither of the methods exhibit the wall heating error. However, there are still small oscillations present in the solution computed with the WENO-Noh scheme, and the shock front is much more smeared than that of the solution computed with WENO- C - W .

Finally, comparing Fig.11 and Fig.13, we see that the wall viscosity for the energy equation has properly aligned the forcing terms $\mathcal{H}(\rho)$, $\mathcal{H}(\rho u)$ and $\mathcal{H}(E)$. Realignment of the gradient of fluxes removes the wall-heating problem, created by the smearing of the shock fronts. The artificial viscosity term (33) is responsible for this realignment.

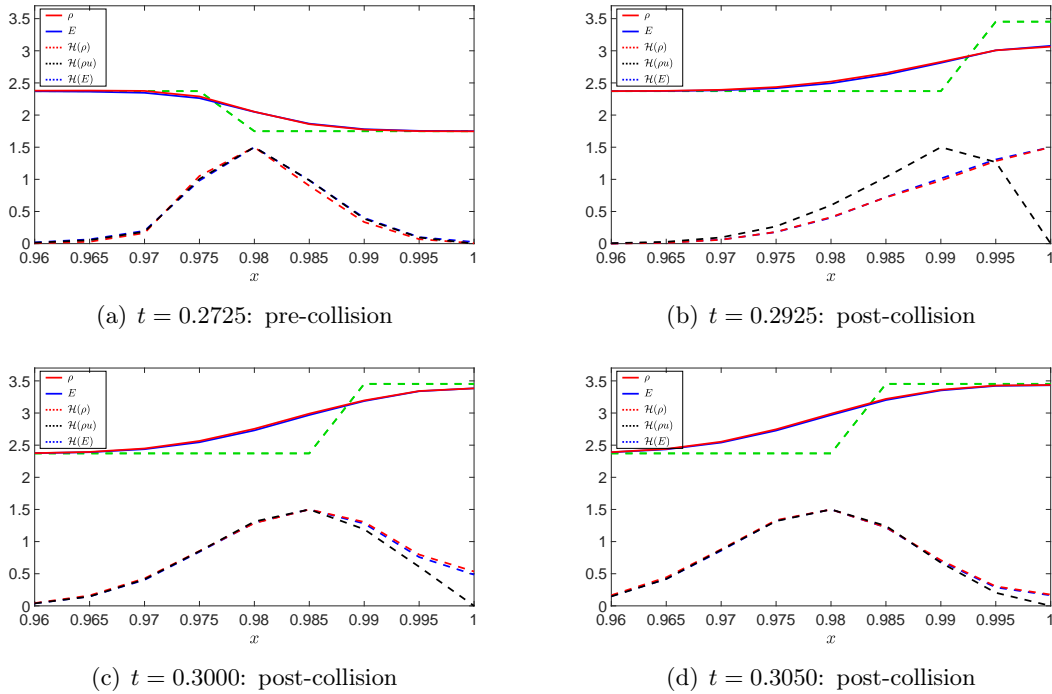


Figure 13: Comparison of the energy and energy forcing term $\mathcal{H}(E)$ (blue/blue dashed) with the density, suitably resized, and the density forcing term $\mathcal{H}(\rho)$ (red/red dashed) and the momentum forcing term $\mathcal{H}(\rho u)$ (black dashed) for the Sod shock tube problem with the wall viscosity activated for the momentum and energy equations. The green dashed curve is the exact solution. The figures shown are zoomed in at the shock just before or just after the shock front has collided with the wall at $x = 1$.

5.2.3 Noise removal with the noise indicator

We now employ our noise indicator algorithm to the Sod shock tube problem with the aim of removing the noise present in the velocity profile at the contact discontinuity.

In the test below, we employ our WENO- $C-N$ scheme with η chosen such that $\eta\Delta\tau/\Delta x^2 = 0.005$ in the heat equation used for noise removal; an explicit time-stepping scheme is used and only one time-step is taken. For the noise detection algorithm, C_{ref} in (28) is computed using $\delta h = 0.0001$. Fig.14(b) shows that the noise indicator removes the spurious oscillations from the velocity profile. The localized diffusion mechanism ensures that the solution in other regions is unchanged, and this is demonstrated in Fig.14(a). We note that the noise indicator algorithm affects neither the sharpness of the shock front nor the speed of the shock, nor the order of the numerical method (which we shall show results for below).

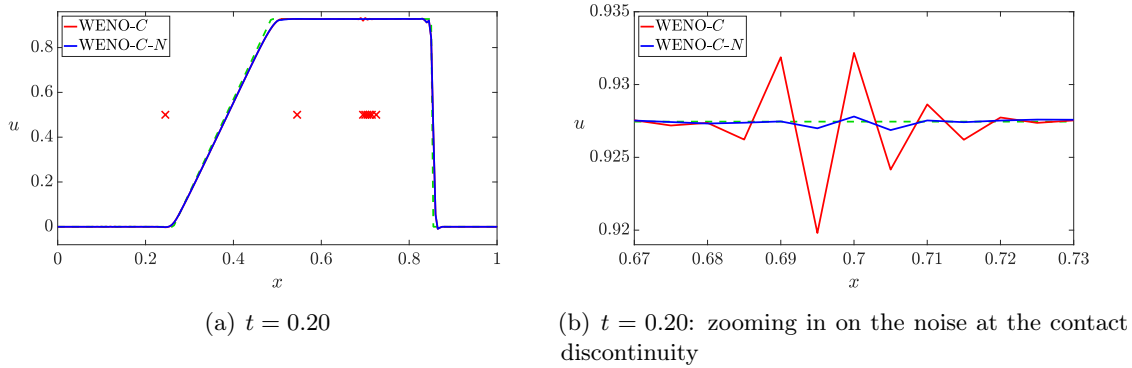
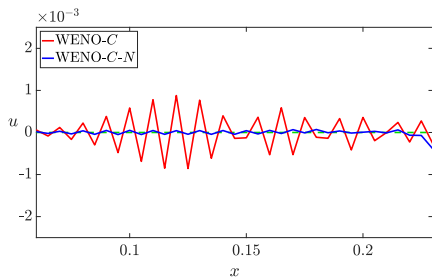


Figure 14: Comparison of the velocity profiles for the Sod shock tube problem computed with WENO-C and WENO-C-N with 201 cells. The red crosses in Fig.14(a) indicate where the function $\mathbb{1}_{\text{noise}}(x)$ is active.



There is also high-frequency noise present to left of the expansion wave (shown in the figure to the left); again, the noise indicator detects and removes this noise.

In Fig.15(a), we show the velocity profile, computed using the WENO-C-W-N scheme, after the shock-wall collision. Here, all of the post-collision noise is damped by the wall viscosity. The WENO-C-W-N scheme removes spurious oscillations in the solution, while ensuring that a sharp shock front and the correct wave speed are retained, even after multiple shock-wall collisions, as shown in Fig.15(b).

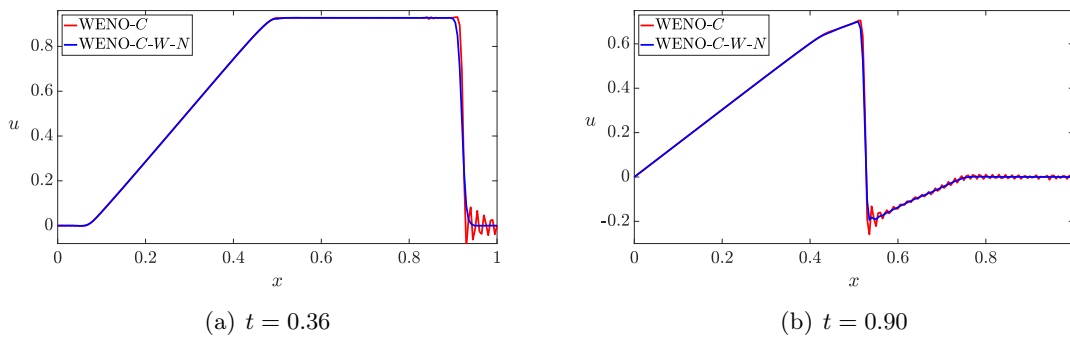


Figure 15: Comparison of the velocity solution profile produced using WENO-C and WENO-C-W-N for the post-collision bounce-back in the Sod shock tube problem with 201 cells.

5.2.4 Error analysis and convergence tests

We now compare the errors of the various numerical schemes given in Table 12 in Appendix A applied to the Sod shock-wall collision and bounce-back problem. The solutions are com-

puted with all parameters fixed across the different methods, giving an objective evaluation of each scheme.

As advised by Greenough & Rider [15], and in order to fairly compare our results with those found in the numerics literature, we use the CFL number equal to 0.6. We have found that the use of a smaller CFL number of 0.3 does not (appreciably) change the conclusions of our numerical tests. For instance, the solutions produced using WENO and WENO- C - W - N show (roughly) the same relative error and order of convergence when CFL=0.3 as they do when CFL=0.6. However, the presence of the nonlinear artificial viscosity terms in the Euler- C equations, when combined with an explicit time-integration scheme, place restrictions on the CFL number that would otherwise not be present in the stand-alone WENO algorithm. In particular, for the Sod test problem, due to the additional artificial viscosity present during the shock-wall collision phase, we have found an upper bound on the CFL number to be ≈ 0.7 . While our stand-alone WENO scheme is (formally) stable for much larger CFL numbers, the relative error and the order of convergence degrades as the CFL number is increased. Indeed, it is demonstrated by Greenough & Rider [15] that only 75% of the fifth-order convergence rate of WENO is achieved when CFL=1.0, whereas the full fifth-order convergence is achieved for CFL=0.6. Therefore, the use of the smaller CFL=0.6 is also necessary for the stand-alone WENO scheme.

Scheme		Cells			
		101	201	401	801
WENO	Error	1.662×10^{-2}	1.772×10^{-2}	1.086×10^{-2}	8.214×10^{-3}
	Order	–	-0.093	0.706	0.403
WENO- $ u_x $	Error	1.534×10^{-2}	1.441×10^{-2}	8.444×10^{-3}	5.864×10^{-3}
	Order	–	0.090	0.771	0.526
WENO-Noh	Error	3.436×10^{-2}	1.799×10^{-2}	9.117×10^{-3}	4.795×10^{-3}
	Order	–	0.934	0.980	0.927
WENO- N	Error	1.667×10^{-2}	1.666×10^{-2}	1.064×10^{-2}	7.262×10^{-3}
	Order	–	0.001	0.648	0.550
WENO- C	Error	1.520×10^{-2}	1.160×10^{-2}	6.453×10^{-3}	3.927×10^{-3}
	Order	–	0.390	0.846	0.717
WENO- C - N	Error	1.504×10^{-2}	1.134×10^{-2}	6.412×10^{-3}	3.780×10^{-3}
	Order	–	0.407	0.823	0.763
WENO- C - W	Error	1.990×10^{-2}	1.151×10^{-2}	5.774×10^{-3}	3.019×10^{-3}
	Order	–	0.790	0.995	0.936
WENO- C - W - N	Error	1.983×10^{-2}	1.146×10^{-2}	5.770×10^{-3}	3.018×10^{-3}
	Order	–	0.791	0.990	0.935

Table 4: Post shock-wall collision ($t = 0.36$) L^1 error of the computed velocity minus the exact solution and convergence for the Sod problem with shock-wall collision and bounce-back.

In Table 4, we list the L^1 error of the computed velocity minus the exact solution, and study the order of convergence for the Sod problem with shock-wall collision and bounce-back. WENO- C produces solutions that are significantly better than those produced with WENO- $|u_x|$, which are significantly better than those solutions produced with the stand-

alone WENO algorithm. Note that the use of the noise removal algorithm consistently improves the error bounds, while maintaining the order of accuracy.

On the coarser grids containing 101 or 201 cells, the WENO- $C-W$ and WENO- $C-W-N$ schemes produce solutions with slightly larger errors than the solution produced with WENO- $C-N$; this is caused by the slight smearing of the shock, post wall collision. The solutions are, however, *qualitatively* significantly better, as evidenced by Fig.12 and Fig.15 above, as well as Fig.16 below. Both WENO- $C-W$ and WENO- $C-W-N$ maintain a relatively high order of accuracy, whereas the presence of the post-collision noise ensures that both WENO and WENO- $|u_x|$ have convergence rates that are irregular and relatively poor.

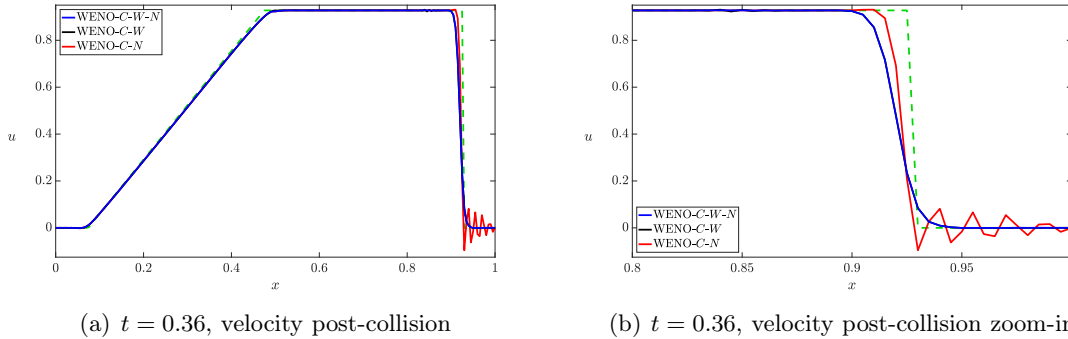


Figure 16: Comparison of the velocity solution profile produced using WENO- $C-W-N$, WENO- $C-W$, and WENO- $C-N$ for the post-collision bounce-back in the Sod shock tube problem with 201 cells.

We remark that our conclusions described above do not change if we replace the L^1 norm with either the L^2 or L^∞ norms. We list in Table 5 the L^2 and L^∞ error analysis for the post shock-wall collision velocity for the Sod problem, where the velocity is computed using either WENO- $|u_x|$ or WENO- $C-W-N$.

For the L^2 error analysis, we first note the odd behavior for WENO- $|u_x|$ on the coarser grids with 101 and 201 cells. The increase in the L^2 error despite mesh refinement is caused by the base WENO scheme; referring to Table 4, we see that the L^1 error of solutions produced with WENO increases as the mesh is refined from 101 to 201 cells. This phenomenon is due to the large oscillations that occur post shock-wall collision. The WENO- $C-W-N$ scheme removes these oscillations, at the cost of a slight smearing of the shock front; this smearing results in a larger L^2 error on coarse grids when compared with WENO- $|u_x|$, but smaller L^2 errors and better rates of convergence as the mesh is refined.

Table 5 shows that the L^∞ errors for both WENO- $|u_x|$ and WENO- $C-W-N$ grow as the mesh is refined. As noted in [15], this is due to the localization of the error at the shock. However, we remark that the L^∞ errors for WENO- $C-W-N$ are smaller than the L^∞ errors for WENO- $|u_x|$ on the grids with 201, 401, and 801 cells; moreover, these errors grow at a faster rate for WENO- $|u_x|$ than for WENO- $C-W-N$.

In addition to the figures and qualitative evidence provided, the L^1 , L^2 , and L^∞ error studies indicate that the C -method produces highly accurate solutions with close to optimal rates of convergence for the Sod shock-wall collision and bounce-back test.

Norm	Scheme		Cells			
			101	201	401	801
L^2	WENO- $ u_x $	Error	4.775×10^{-2}	6.068×10^{-2}	4.640×10^{-2}	3.765×10^{-2}
		Order	-	-0.346	0.387	0.302
	WENO- $C-W-N$	Error	6.953×10^{-2}	6.098×10^{-2}	4.423×10^{-2}	3.324×10^{-2}
		Order	-	0.189	0.463	0.412
L^∞	WENO- $ u_x $	Error	4.262×10^{-1}	7.417×10^{-1}	8.024×10^{-1}	8.925×10^{-1}
		Order	-	-0.799	-0.113	-0.154
	WENO- $C-W-N$	Error	5.663×10^{-1}	6.926×10^{-1}	7.124×10^{-1}	7.456×10^{-1}
		Order	-	-0.290	-0.041	-0.066

Table 5: Post shock-wall collision ($t = 0.36$) L^2 and L^∞ error of the computed velocity minus the exact solution and convergence for the Sod problem with shock-wall collision and bounce-back.

5.2.5 Comparison with other schemes

For the purposes of benchmarking our WENO and WENO- N schemes prior to shock-wall collision, we present error analysis and convergence rates comparing our simplified WENO scheme with the scheme utilized by Greenough and Rider in [15]. The WENO scheme that is presented in [15] is formally fifth-order accurate in space, with time integration done using a total variation diminishing (TVD) third-order Runge-Kutta method. Flux-splitting is accomplished using a method similar to the Lax-Friedrichs flux-splitting (see [15] for the details). We will refer to this method as RK3-WENO5.

The error norm utilized in [15] is of the form

$$\|\rho(\cdot, t) - \rho^*(\cdot, t)\|_{L_{GR}^1} := \frac{1}{M} \sum_{i=1}^M \frac{|\rho(x_i, t) - \rho^*(x_i, t)|}{|\rho^*(x_i, t)|},$$

where ρ is the computed density and ρ^* is the exact solution for the density. We will refer to this norm as the L_{GR}^1 norm.

In Table 6, we calculate the L_{GR}^1 errors for the density for the Sod shock tube problem computed with WENO and WENO- N , and compare them with the corresponding values in [15]. All simulations were run with a CFL number of 0.6. We see that our simplified WENO scheme and noise indicator algorithm compare well with the more complicated RK3-WENO5 scheme. Consequently, using our simplified WENO algorithm for the purposes of comparison in our error analysis for the artificial viscosity methods presented is justified; that is to say, comparing the performance of our artificial viscosity methods with our simplified WENO scheme is similar to comparing the performance of our artificial viscosity methods with the more complicated (and ‘industry-standard’) RK3-WENO5.

Scheme		Cells		
		101	201	401
WENO	Error	1.57×10^{-2}	7.93×10^{-3}	4.49×10^{-3}
	Order	–	0.99	0.82
WENO-N	Error	1.60×10^{-2}	7.90×10^{-3}	4.37×10^{-3}
	Order	–	1.02	0.85
RK3-WENO5	Error	1.58×10^{-2}	8.24×10^{-3}	4.47×10^{-3}
	Order	–	0.93	0.88

Table 6: Pre shock-wall collision ($t = 0.20$) L_{GR}^1 error analysis and convergence tests for the density for the Sod shock tube problem.

5.3 The Noh problem

As a further example of wall-heating, we next consider the classical 1- D planar Noh problem [37, 25]. The domain of interest is $-0.5 \leq x \leq 0.5$, the adiabatic constant is $\gamma = 5/3$, and the initial data is given by

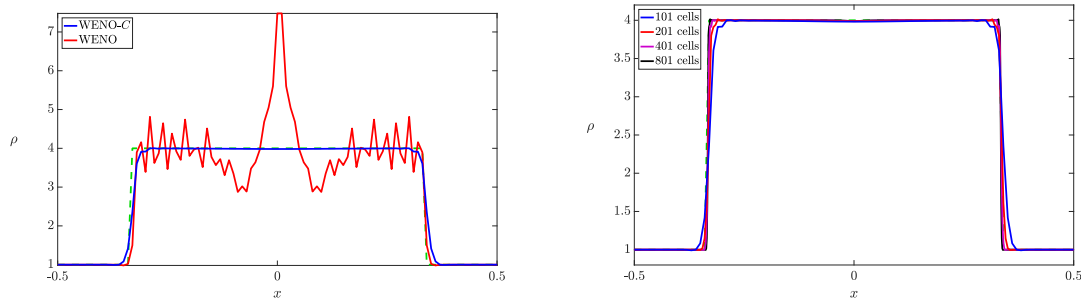
$$\begin{bmatrix} \rho_0 \\ (\rho u)_0 \\ E_0 \end{bmatrix} = \begin{bmatrix} 1 \\ 1 \\ 0.5 + \frac{10^{-6}}{\gamma-1} \end{bmatrix} \mathbb{1}_{[-0.5,0)}(x) + \begin{bmatrix} 1 \\ -1 \\ 0.5 + \frac{10^{-6}}{\gamma-1} \end{bmatrix} \mathbb{1}_{[0,0.5]}(x).$$

The solution for this problem consists of two infinite strength shocks propagating with speed $1/3$ outwards from the origin, with a state of constant density and pressure left behind.

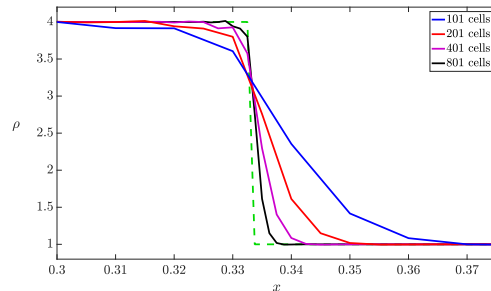
As demonstrated in [25], most schemes tend to produce the anomalous wall-heating at the center origin. We shall utilize our WENO- C method (i.e. no shock-wall collision algorithm) with 101 cells. We choose the relevant parameters as

$$\beta^u = 1.0, \quad \beta^E = 10.0, \quad \varepsilon = 50.0, \quad \kappa = 1.0.$$

The value of β^u is chosen large enough to eliminate post-shock oscillations, while β^E is chosen to minimize the wall-heating. In Fig.17, we compare the solutions computed using WENO and WENO- C ; it is clear that WENO- C produces a much more accurate solution, with the post-shock oscillations and wall-heating eliminated.



(a) $t = 1.0$: density, comparison of WENO- C and WENO
 (b) $t = 1.0$: density, comparison of WENO- C with different grid spacings



(c) $t = 1.0$: density zoom-in at the shock, comparison of WENO- C with different grid spacings

Figure 17: The density profile at time $t = 1.0$ for the Noh problem, with the solution computed using (a) WENO or (b,c) WENO- C . The dashed green curve is the exact solution.

5.4 The LeBlanc shock tube problem

We now turn our attention to the LeBlanc shock tube problem. Here, the domain of interest is $0 \leq x \leq 9$, the adiabatic constant is $\gamma = \frac{5}{3}$, and the initial data is given by

$$\begin{bmatrix} \rho_0 \\ (\rho u)_0 \\ E_0 \end{bmatrix} = \begin{bmatrix} 1 \\ 0 \\ 10^{-1} \end{bmatrix} \mathbb{1}_{[0,3)}(x) + \begin{bmatrix} 10^{-3} \\ 0 \\ 10^{-9} \end{bmatrix} \mathbb{1}_{[3,9)}(x).$$

The large jump in the initial energy E_0 produces a very strong shock wave, making the LeBlanc shock-tube problem a very difficult test case. Most numerical schemes tend to produce large overshoots in the internal energy at the contact discontinuity, which results in a loss of accuracy in the shock speed, as shown in Fig.18. This overshoot in the internal energy is in fact an example of wall-heating; a small undershoot in the density and the continuity of the pressure at the contact produce this observed overshoot in the internal energy. We refer the reader to [40, 26, 30] for further details.

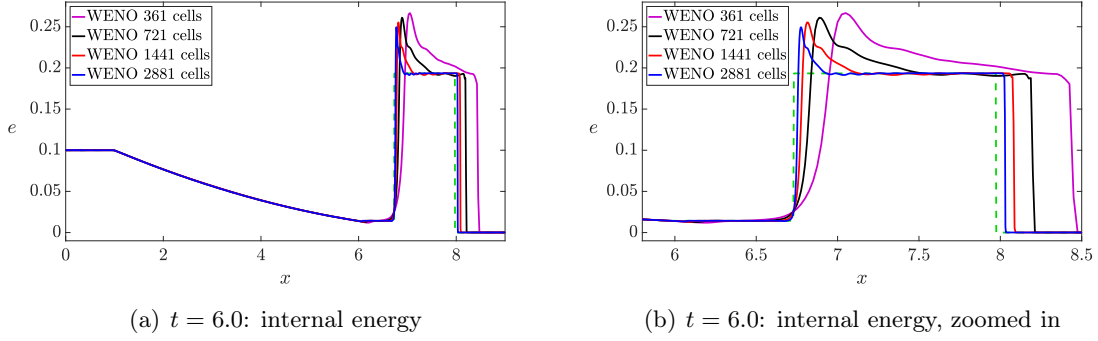


Figure 18: The internal energy profile at time $t = 6.0$ for the LeBlanc shock tube problem, with the solution computed using WENO. The dashed green curve is the exact solution.

Our strategy is to add an additional diffusion term to the right-hand side of the energy equation (13c) that will serve to remove the large overshoot in the internal energy at the contact discontinuity. Specifically, we solve an additional C -equation for a variable C^e forced by $|\partial_x e|/\max_x |\partial_x e|$. Thus, equation (13c) is replaced by

$$\partial_t E + \partial_x(uE + up) = \partial_x \left(\mathcal{B}^{(E)}(t) \rho C \partial_x(E/\rho) \right) + \partial_x \left(\mathcal{B}^{(e)}(t) \rho C^e \partial_x(E/\rho) \right), \quad (35)$$

where the function C^e is computed using

$$\partial_t C^e + \frac{S(\mathbf{u})}{\varepsilon_e \Delta x} C^e - \kappa_e \Delta x \cdot S(\mathbf{u}) \partial_{xx} C^e = \frac{S(\mathbf{u})}{\varepsilon_e \Delta x} G^e. \quad (36)$$

The artificial viscosity coefficients are given by (14) and

$$\mathcal{B}^{(e)}(t) = (\Delta x)^2 \cdot \frac{\max_x |\partial_x u|}{\max_x C^e} (\beta^e + \beta_w^e \cdot \overline{C}_w(t)),$$

and C , $C_w(x, t)$, and $\overline{C}_w(t)$ are defined by (13d), (13e), and (15), respectively. The forcing to the C^e equation (36) is

$$G^e(x, t) = \mathbb{1}_{(0, \infty)}(\partial_x u) \frac{|\partial_x e|}{\max_x |\partial_x e|}.$$

Here, the indicator function $\mathbb{1}_{(0, \infty)}(\partial_x u)$ represents an *expansion switch*, in which G^e is non-zero only if $\partial_x u > 0$.

5.4.1 Stabilizing shock-wall collision

To simulate the collision of the shock-wave with the wall, we use solid wall boundary conditions (16). Motivated by the results for the Sod shock tube problem presented in 5.2.1, we add wall viscosity to the momentum and energy equations; we choose the parameters as

$$\begin{aligned} \beta^u &= 0.001, & \beta^E &= 0.0, & \beta^e &= 0.4, & \beta_w^u &= 4.0, & \beta_w^E &= 0.0, & \beta_w^e &= 0.0, \\ \varepsilon &= 1.25, & \kappa &= 10.0, & \varepsilon_e &= 1.25, & \kappa_w &= 14.0, & \varepsilon_w &= 50.0, & \kappa_w &= 4. \end{aligned}$$

We employ our WENO-*C-W* scheme with 721 cells. Since this is a more challenging problem than the Sod shock tube problem, we use the smaller CFL number of 0.25.

For the purpose of comparison, we also implement the WENO-Noh scheme, with the parameters in (40) set as $\beta_{\text{Noh}}^u = 8.0$ and $\beta_{\text{Noh}}^E = 9.0$. These parameters were chosen with the aim of suppressing post-collision noise while preventing the occurrence of the wall heating error. We remark that WENO-Noh failed for CFL=0.25, and required the much smaller CFL ≈ 0.045 to run.

The shock-wave moves to the right and collides with the right wall at time $t \approx 7.2$. Prior to shock collision, the WENO-Noh scheme produces a solution with an overshoot in the internal energy at the contact discontinuity. This results in an incorrect shock front and wave speed. The viscosity for the momentum at the shock and the energy at the contact discontinuity in our WENO-*C-W* scheme remove post-shock oscillations and the overshoot in the internal energy, respectively, as shown in Fig.19.

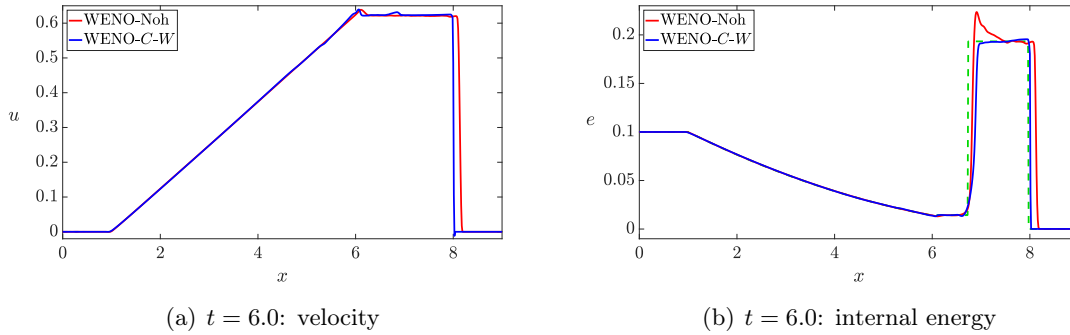


Figure 19: The (a) velocity and (b) internal energy profiles for the LeBlanc shock tube problem before the collision with the wall. The solution is computed with viscosity activated for the momentum and energy equations.

Post shock-wall collision, the wall viscosity for the momentum and energy equations damp-out the oscillations behind the shock, while ensuring that the solution maintains a sharp shock front and the correct shock speed (see Fig.20). Moreover, the wall viscosity for the energy equation prevents the wall heating error from occurring, as shown in Fig.20(d). Due to the lack of smoothness of the localizing artificial viscosity coefficient $|\partial_x u|$, the WENO-Noh scheme is unable to fully suppress all the post-collision oscillations, though the heat conduction term in the energy equation prevents the wall heating error from occurring. In Fig.20(c), we zoom in on the internal energy profile near the wall; it is evident that the solution computed with WENO-*C-W* is better than that computed with WENO-Noh, but there is a small error between the computed solution and the exact solution. This error occurs because of a very small inaccuracy in the density profile, shown in Fig.20(d). Since the density is so small here, and since the internal energy is given by (7), even tiny errors are greatly amplified, making it very difficult to get a completely accurate solution for the internal energy.

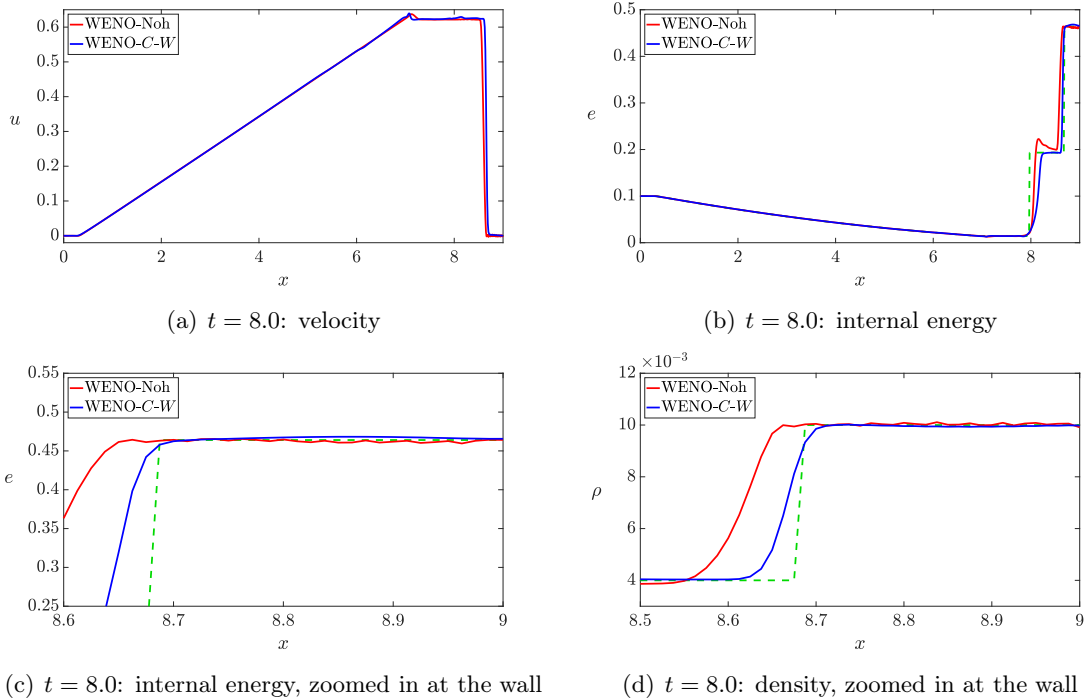


Figure 20: The (a) velocity, (b) internal energy, (c) zoomed in internal energy and (d) zoomed in density profiles for the LeBlanc shock tube problem after the collision with the wall. The solution computed with WENO-C-W has the wall viscosity activated for the momentum and energy equations.

5.4.2 Error analysis and convergence tests

We now compare the errors of the various numerical schemes listed in Table 12 applied to the LeBlanc shock tube problem, with the various relevant parameters fixed across the different methods. The L^1 errors in the velocity are computed using formula (31a), and are listed in Table 7 (time $t = 6.0$) and Table 9 (time $t = 8.0$). All of the simulations were run with a CFL number of 0.25, except for WENO-Noh, which required $CFL \approx 0.045$.

Prior to shock-wall collision, it is evident from Table 7 that the C -method produces a solution that is significantly better than those solutions produced without the C -method. The L^1 errors for the velocity computed using WENO- C are almost an order of magnitude smaller than the L^1 errors for the velocity computed using WENO and WENO-Noh. This is primarily due to the removal of the overshoot in the internal energy, which results in an accurate shock speed.

On the other hand, the removal of the overshoot in the internal energy through the use of C^e results in a more smeared contact discontinuity, as shown in Fig.19(b). The smearing of the contact discontinuity results in a non-physical “bump” appearing in the velocity profile, as shown in Fig.19(a). Note that this bump does not appear in the velocity profile computed using WENO-Noh, since in this case the contact discontinuity is sharper, at the expense of a large overshoot in the internal energy. We suggest, however, that this defect in the solution computed using C^e is relatively insignificant when compared against

the magnitude of the error in the internal energy solutions computed without C^e . This is primarily due to the fact that the internal energy error results in a highly inaccurate shock speed which, in turn, leads to a highly inaccurate solution, as evidenced by Table 7. On the other hand, the velocity bump error arises from the correction of the overshoot in the internal energy, and subsequently the shock speed and location; the latter two corrections result in a much more accurate solution overall, again demonstrated in Table 7. Moreover, we note that the bump error decreases with mesh refinement approximately four times as fast as the overshoot error, as shown in Table 8. Here, the overshoot/bump error is computed by calculating the difference between the value at the peak of the overshoot/bump and the value of the exact solution there⁵.

Scheme		Cells			
		361	721	1441	2881
WENO	Error	3.469×10^{-2}	1.659×10^{-2}	8.010×10^{-3}	4.016×10^{-3}
	Order	–	1.065	1.050	0.996
WENO-Noh	Error	2.546×10^{-2}	1.239×10^{-2}	6.001×10^{-3}	3.010×10^{-3}
	Order	–	1.040	1.045	0.996
WENO-N	Error	3.468×10^{-2}	1.661×10^{-2}	8.015×10^{-3}	4.022×10^{-3}
	Order	–	1.062	1.051	0.995
WENO-C	Error	7.190×10^{-3}	3.959×10^{-3}	2.008×10^{-3}	1.096×10^{-3}
	Order	–	0.864	0.976	0.873
WENO-C-N	Error	7.169×10^{-3}	3.881×10^{-3}	2.007×10^{-3}	1.113×10^{-3}
	Order	–	0.885	0.951	0.851

Table 7: Pre shock-wall collision ($t = 6.0$) L^1 error analysis and convergence tests for the velocity for the LeBlanc shock tube problem.

Scheme		Cells			
		361	721	1441	2881
WENO	Overshoot Error	7.330×10^{-2}	6.780×10^{-2}	6.200×10^{-2}	5.620×10^{-2}
	Order	–	0.113	0.129	0.142
WENO-C	Bump Error	1.500×10^{-2}	9.700×10^{-3}	6.600×10^{-3}	3.900×10^{-3}
	Order	–	0.629	0.556	0.759

Table 8: Comparison of the overshoot error in the internal energy and the bump error in the velocity for solutions to the LeBlanc shock tube problem at time $t = 6.0$.

We note here that Table 7 seems to suggest that the WENO and WENO-Noh schemes produce solutions that converge at first-order, even though the solutions computed using these schemes are very poor, as shown, for example, in Fig.18. This “super-convergence” [19] is due to large errors on coarser meshes, rather than smaller errors on finer meshes,

⁵This error is thus a *local* L^∞ error.

and is therefore superficial. On the other hand, the WENO- C and WENO- $C-N$ schemes produce solutions with much smaller errors, and suggest close to first-order convergence.

Post shock-wall collision, the wall C -method produces a highly accurate non-oscillatory solution, while ensuring that the wall heating error does not occur. While the WENO-Noh scheme is able to suppress most of the oscillations, the large amount of viscosity needed due to the lack of smoothness of $|\partial_x u|$ results in a shock front that is too smeared, as well as the imposition of a smaller time-step. Again, we see that the noise indicator algorithm serves primarily as an error correction mechanism, removing small-scale high-frequency oscillations from the solution.

Scheme		Cells			
		361	721	1441	2881
WENO	Error	2.160×10^{-2}	9.832×10^{-3}	5.336×10^{-3}	2.896×10^{-3}
	Order	–	1.136	0.882	0.882
WENO-Noh	Error	1.528×10^{-2}	6.544×10^{-3}	3.407×10^{-3}	1.668×10^{-3}
	Order	–	1.224	0.942	1.030
WENO- N	Error	2.141×10^{-2}	9.684×10^{-3}	5.178×10^{-3}	2.793×10^{-3}
	Order	–	1.144	0.903	0.891
WENO- C	Error	5.703×10^{-3}	3.486×10^{-3}	2.024×10^{-3}	1.052×10^{-3}
	Order	–	0.710	0.785	0.944
WENO- $C-N$	Error	5.627×10^{-3}	3.384×10^{-3}	2.001×10^{-3}	1.045×10^{-3}
	Order	–	0.734	0.758	0.937
WENO- $C-W$	Error	6.077×10^{-3}	3.170×10^{-3}	1.694×10^{-3}	8.257×10^{-4}
	Order	–	0.939	0.904	1.037
WENO- $C-W-N$	Error	6.064×10^{-3}	3.143×10^{-3}	1.703×10^{-3}	8.363×10^{-4}
	Order	–	0.948	0.884	1.026

Table 9: Post shock-wall collision ($t = 8.0$) L^1 error analysis and convergence tests for the velocity for the LeBlanc shock tube problem.

5.5 The Peak shock tube problem

We next consider the Peak shock tube problem, introduced in [25]. The domain of interest is $0.1 \leq x \leq 0.6$, the adiabatic gas constant is $\gamma = 1.4$, and the initial data is given by

$$\begin{bmatrix} \rho_0 \\ (\rho u)_0 \\ E_0 \end{bmatrix} = \begin{bmatrix} 0.1261192 \\ 11.1230540 \\ 1.962323 \times 10^3 \end{bmatrix} \mathbb{1}_{[0.1,0.5)}(x) + \begin{bmatrix} 6.591493 \\ 14.932505 \\ 24.800422 \end{bmatrix} \mathbb{1}_{[0.5,0.6]}(x).$$

The difficulty in simulating solutions to Peak is due to the fact that the shock wave moves significantly slower than the expansion wave; moreover, the distance between the contact discontinuity and the shock is very small, resulting in a sharp and narrow peak in the density. Most schemes produce inaccurate velocity profiles with large overshoots and low-frequency noise at the expansion wave [25, 15].

The stand-alone WENO scheme produces a similarly poor velocity profile, but the C -method can be used to produce a good solution. Since the noise appears in the velocity

profile in the region with the rarefaction wave, and since the usual C -method includes a compression switch so that artificial viscosity is active only in regions of compression, we employ an additional C -equation for the rarefaction wave, whose solution is $C^r(x, t)$. We consider the following modification to (13b):

$$\begin{aligned} \partial_t(\rho u) + \partial_x(\rho u^2 + p) &= \partial_x \left(\rho \left(\tilde{\beta}^u C + \tilde{\beta}^r C^r \right) \partial_x u \right), \\ \partial_t C^r + \frac{S(\mathbf{u})}{\varepsilon \Delta x} C^r - \kappa \Delta x \cdot S(\mathbf{u}) \partial_{xx} C^r &= \frac{S(\mathbf{u})}{\varepsilon \Delta x} G^r, \end{aligned}$$

where C is the solution to (13d), and where $\tilde{\beta}^u = \frac{\max_x |\partial_x u|}{\max_x C} \beta^u$ and $\tilde{\beta}^r = \frac{\max_x |\partial_x u|}{\max_x C^r} \beta^r$, with

$$G^r(x, t) = \mathbb{1}_{(0, +\infty)}(\partial_x u) \cdot \frac{|\partial_x u(x, t)|}{\max_x |\partial_x u(x, t)|}.$$

We remark that we have omitted the wall function \bar{C}_w since we are not simulating the shock-wall collision for this problem.

WENO and WENO- C (with the above modification) are used on a grid with 801 cells and with a time-step $\Delta t \approx 3.55 \times 10^{-6}$, giving CFL=0.6. The final time is $t = 0.0039$, and the results are shown in Fig.21. The relevant parameters are chosen as

$$\beta^u = 1.0, \quad \beta^r = 10.0, \quad \varepsilon = 10.0, \quad \kappa = 40.0, \quad \varepsilon_r = 1.0, \quad \kappa_r = 20.0.$$

As shown in Fig.21, the extra viscosity provided by β^r at the rarefaction wave removes the large overshoot and low frequency non-physical oscillations that are present in the solution produced with WENO.

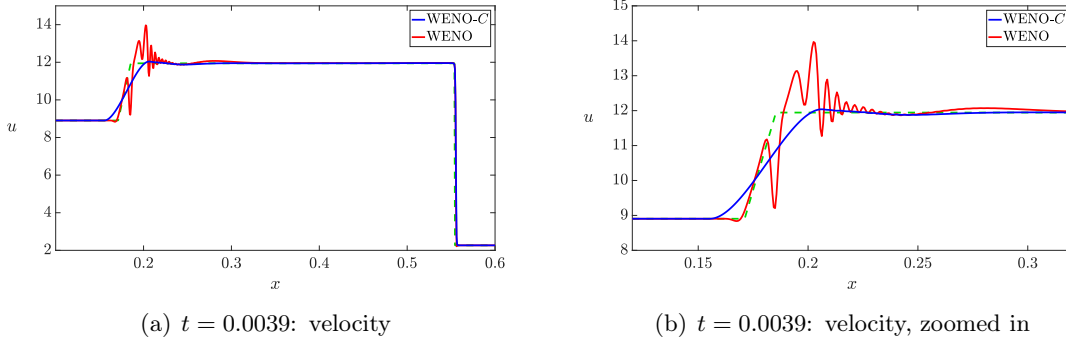


Figure 21: Comparison of WENO and WENO- C for the Peak shock tube problem with 801 cells. The green curve is the exact solution.

In [25], an error analysis of various schemes applied to the Peak shock tube problem with the above specifications is provided. We compute the L^1 and L^2 errors for the computed velocity minus the exact solution, using (31a) for the L^1 error and

$$\|u(\cdot, t) - u^*(\cdot, t)\|_{L^2} = \sqrt{\frac{1}{M} \sum_{i=1}^M |u(x_i, t) - u^*(x_i, t)|^2},$$

where M is the number of cells used in the simulation and u^* is the exact solution. Following [25], we list the errors in percentage form with the ratio in question given by $\frac{\|u-u^*\|}{\|u^*\|}$. We also list the smallest error computed from all the schemes considered in [25]; namely, the error computed from the scheme of Liu and Lax [27, 28], which we will refer to as LL. We see in Table 10 that WENO- C compares very well with LL, with the solution producing smaller errors in both the L^1 and L^2 norms.

Norm	Scheme		Cells 801
$\ u - u^*\ _{L^1}$	WENO	Error %	1.057×10^{-1} 1.0 %
	WENO- C	Error %	7.260×10^{-2} 0.7 %
	LL	Error %	– 0.8 %
$\ u - u^*\ _{L^2}$	WENO	Error %	5.168×10^{-1} 4.7 %
	WENO- C	Error %	4.684×10^{-1} 4.3 %
	LL	Error %	– 4.4 %

Table 10: L^1 and L^2 error analysis for the velocity u for the Peak shock tube problem at time $t = 0.0039$.

This test demonstrates the flexibility of the C -method; although a standard WENO scheme produces an inaccurate and oscillatory solution, a very simple modification of the C -method allows for the suppression of these oscillations, resulting in a more accurate solution.

5.6 The Osher-Shu shock tube problem

The Osher-Shu shock tube problem, introduced in [46], simulates a shock front, perturbed by sinusoidal fluctuations. The computational domain is $-1 \leq x \leq 1$, $\gamma = 1.4$, with initial data

$$\begin{bmatrix} \rho_0 \\ (\rho u)_0 \\ E_0 \end{bmatrix} = \begin{bmatrix} 3.857143 \\ 10.14185 \\ 39.1666 \end{bmatrix} \mathbb{1}_{[-1,-0.8)}(x) + \begin{bmatrix} 1 + 0.2 \sin(5\pi x) \\ 0 \\ 2.5 \end{bmatrix} \mathbb{1}_{[-0.8,1]}(x). \quad (37)$$

We employ free-flow boundary conditions (17) at the left wall $x = -1$, and solid wall boundary conditions (16) at the right wall $x = 1$.

5.6.1 Noise removal with the noise indicator

In order to test the efficacy of our noise detection and removal algorithm for the Osher-Shu test, we perform our numerical simulations using too large a time-step and hence a numerically unstable CFL number, which produces spurious high-frequency oscillation behind the

shock⁶. Of course, high-frequency oscillations can be created by numerous numerical instabilities, but an unstable CFL number creates the prototypical oscillation pattern for testing a noise removal scheme.

Our goal is to remove the high-frequency noise from the solution without affecting the low-frequency sinusoidal oscillations that are the main feature of this test problem. To this end, we first compute a solution using WENO with 1025 cells with a time-step $\Delta t = 5.0 \times 10^{-4}$, giving a CFL number of 1.2.

The relatively large number of cells and time-step produce noise with a frequency that is significantly higher than the lower frequency non-spurious oscillations present in the solution. The WENO- N scheme is used with the reference coefficient C_{ref} in (28) calculated using $\delta h = 10^{-3}$. The noise removal viscosity η is chosen such that $\eta \Delta \tau / \Delta x^2 = 0.25$ and only one time-step is taken in the heat equation. Since an exact solution is not available for this problem, our “exact” solution is computed with WENO using 8193 cells and a time-step of $\Delta t = 3.125 \times 10^{-5}$, so that $\text{CFL} \approx 0.6$.

In Fig.22, we compare the solutions computed with WENO and WENO- N . The noise indicator algorithm locates and removes the high-frequency noise present in the solution, without affecting the sinusoidal oscillations. The sharpness of the shock front remains unaffected with the use of the noise indicator, due to the deactivation of noise detection in a small region surrounding the shock.

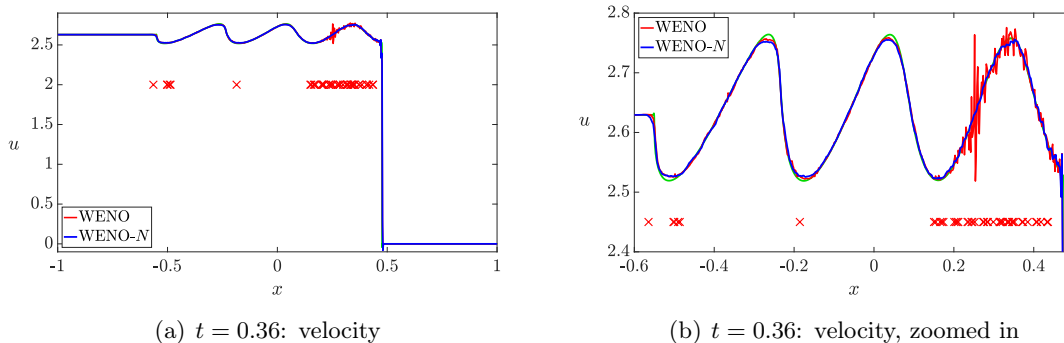


Figure 22: Comparison of WENO and WENO- N for the Osher-Shu problem with 1025 cells. The red crosses indicate where the noise indicator function $\mathbb{1}_{\text{noise}}(x)$ is active. The green curve is the “exact” solution.

For the purpose of benchmarking our noise detection and removal algorithm, we also conduct tests in which we use linear (hyperviscosity) operators (see [20, 50, 5, 38, 3, 4]) of the form

$$(-1)^{r-1} \beta_r (\Delta x)^{2r-1} \frac{\partial^{2r} u}{\partial x^{2r}} \quad (38)$$

to remove noise, where $r \geq 1$. The equations of motion we consider are the Euler equations (4a) with the term (38) on the right-hand side of the momentum equation. When numerically

⁶Artificially inflating the CFL number allows us to model a typical scenario in computational physics in which a DNS-type simulation requires a prohibitively small time-step, and forces simulations that require entering the unstable CFL regime. Our objective is to demonstrate that this high-frequency instability can be suppressed by use of our localized noise removal algorithm.

approximated using our WENO-type discretization, the resulting scheme is referred to as the WENO- $\Delta^r u$ scheme. We perform numerical tests for the WENO- $\Delta^r u$ scheme with $r = 1, 2, 3$, and set $\beta_1 = 0.2$, $\beta_2 = 0.05$, and $\beta_3 = 0.01$, with these values determined *a posteriori* to optimize the resulting solutions.

We compare in Fig.23 the WENO- N and WENO- $\Delta^r u$ simulations; each subfigure shows the computed velocity, obtained using one of the schemes on grids with 513, 1025, 2049, and 4097 cells, as well as the exact solution. The plots shown are zoomed in on the region behind the shock where there is high-frequency noise.

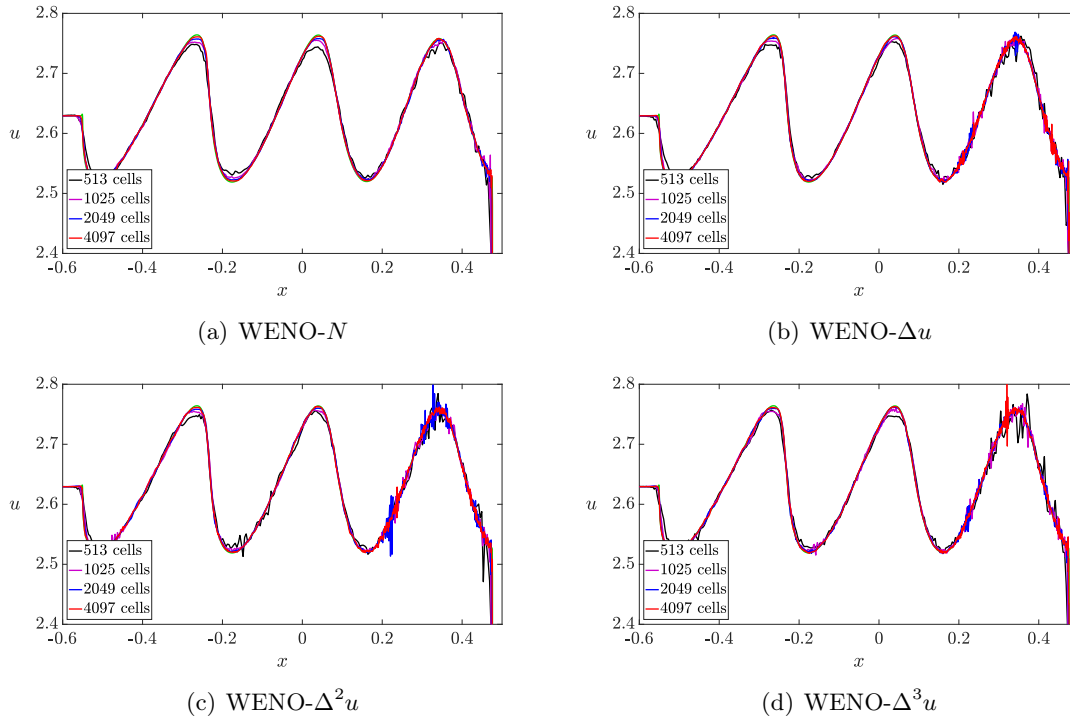


Figure 23: Comparison of the velocity profiles at $t = 0.36$ for the Osher-Shu test. The green curve is the exact solution.

It is clear from these figures that, qualitatively, the WENO- N scheme produces solutions with minimal noise that appear to converge to the exact solution. The hyperviscosity schemes, on the other hand, produce solutions with erratic behavior; for instance, despite mesh refinement, the WENO- $\Delta^3 u$ solution on the 4097 cell grid appears much worse than the solutions on the 1025 and 2049 cell grids. Similarly inconsistent convergence behavior can be observed with WENO- Δu and WENO- $\Delta^2 u$. This is due to the CFL condition violation. It is interesting to observe, on the other hand, that the WENO- N solutions are not subject to this erratic convergence behavior. This is likely the result of the highly localized (in both space and time) nature of the noise detection. Overall, WENO- N appears to produce noise-free, accurate, and convergent solutions.

Defining the L_t^1 norm as

$$\|f\|_{L_t^1} = \frac{1}{KM} \sum_{j=1}^K \sum_{i=1}^M |f(x_i, t_j)|,$$

in Table 11 we compute the L^1 and L_t^1 errors for the velocity at time $t = 0.36$ at various mesh refinements. Once again, we see that the noise indicator algorithm functions as an “error correcter”, reducing the numerical error through the removal of high-frequency noise, while maintaining a relatively high order of accuracy. Among all the schemes considered, WENO- N produces solutions with the smallest errors, providing a quantitative validation of the observations made from Fig.23.

Norm	Scheme		Cells			
			513	1025	2049	4097
$\ \tilde{u}\ _{L^1}$	WENO	Error	1.003×10^{-2}	5.478×10^{-3}	2.018×10^{-3}	1.258×10^{-3}
		Order	–	0.873	1.440	0.682
	WENO- Δu	Error	1.045×10^{-2}	4.717×10^{-3}	1.990×10^{-3}	9.770×10^{-4}
		Order	–	1.148	1.245	1.026
	WENO- $\Delta^2 u$	Error	1.050×10^{-2}	4.774×10^{-3}	2.459×10^{-3}	1.132×10^{-3}
Order		–	1.137	0.957	1.119	
WENO- $\Delta^3 u$	Error	1.084×10^{-2}	4.806×10^{-3}	1.981×10^{-3}	1.109×10^{-3}	
	Order	–	1.174	1.279	0.838	
WENO- N	Error	1.013×10^{-2}	4.432×10^{-3}	1.973×10^{-3}	1.005×10^{-3}	
	Order	–	1.193	1.168	0.973	
$\ \tilde{u}\ _{L_t^1}$	WENO	Error	7.328×10^{-3}	3.223×10^{-3}	1.139×10^{-3}	6.761×10^{-4}
		Order	–	1.185	1.501	0.752
	WENO- Δu	Error	7.484×10^{-3}	3.348×10^{-3}	1.192×10^{-3}	6.418×10^{-4}
		Order	–	1.161	1.490	0.893
	WENO- $\Delta^2 u$	Error	7.333×10^{-3}	3.316×10^{-3}	1.254×10^{-3}	7.255×10^{-4}
Order		–	1.145	1.403	0.789	
WENO- $\Delta^3 u$	Error	7.419×10^{-3}	3.340×10^{-3}	1.196×10^{-3}	6.903×10^{-4}	
	Order	–	1.151	1.482	0.793	
WENO- N	Error	7.066×10^{-3}	3.004×10^{-3}	1.050×10^{-3}	5.656×10^{-4}	
	Order	–	1.234	1.517	0.893	

Table 11: L^1 and L_t^1 error analysis and convergence tests for the velocity u for the Osher-Shu problem at time $t = 0.36$, with $\tilde{u} = u - u^*$ the difference between the computed solution u and the “exact solution” u^* .

We note that the numerical error and the order of convergence remains unchanged when using the density ρ instead of the velocity u ; in particular, the WENO- N algorithm produces solutions with smaller errors and similar rates of convergence as WENO, when errors and

accuracy are computed using ρ . And so, the removal of high-frequency noise in u , in turn, provides a density field that is also free of high-frequency oscillations (c.f. Remark 1).

5.6.2 Stabilizing shock-wall collision for Osher-Shu

We now turn to the issue of stabilizing shock-wall collision for the Osher-Shu problem. The problem is set up as follows: the initial data is (37), the time-step is given by $\Delta t = 5 \times 10^{-4}$ with final time $t = 0.63$, and the number of cells is 512, so that the CFL number is 0.6. We impose the solid wall boundary conditions (23) at the right boundary $x = 1$, and free-flow boundary conditions (22) at the left boundary $x = -1$. The shock-wave moves to the right and collides with the wall at $x = 1$ at time $t \approx 0.5$. Post-collision, there is a large amount of noise present in the solution behind the shock-wave, and our aim is to remove the noise while preserving the sharpness of the shock front and minimizing the damping of the post-shock low frequency oscillations.

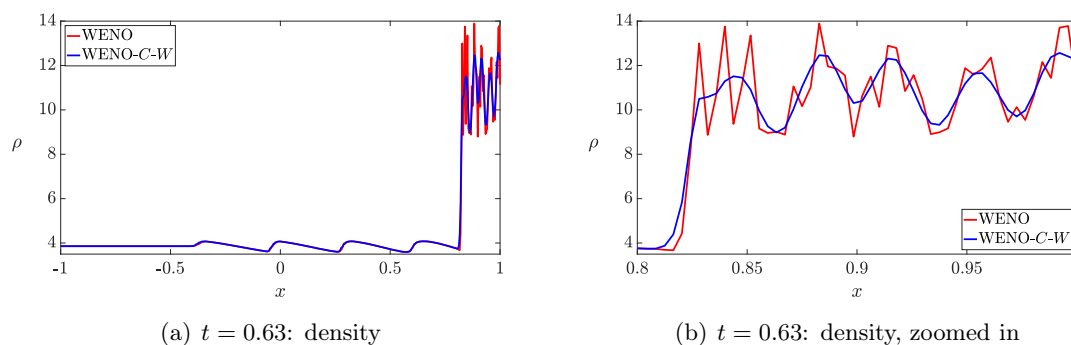


Figure 24: Comparison of WENO vs. WENO- C - W for the density just after the shock-wall collision problem for the Osher-Shu problem with 512 cells.

We employ our WENO- C - W scheme and choose the relevant parameters as

$$\begin{aligned} \beta^u &= 1.0, & \beta^E &= 0.0, & \beta_w^u &= 2.5, & \beta_w^E &= 0.85 \\ \varepsilon &= 1.0, & \kappa &= 5.0, & \varepsilon_w &= 40.0, & \kappa_w &= 4.0. \end{aligned}$$

The results are shown in Fig.24. Post shock-wall collision, WENO produces a noisy solution with high frequency noise interfering with the sinusoidal oscillations, while WENO- C - W produces a solution with a sharp front and without noise.

6 Concluding remarks

In this paper, we have presented three ideas: the first is a space-time smooth artificial viscosity method that is versatile and simple to implement; the second is a shock-wall collision scheme that can be used to suppress post-collision noise that occurs when a shock-wave collides with a fixed boundary and bounces-back; the third is a wavelet-based noise detection and removal scheme that is highly localized and can be used to remove noise present in

solutions. We have demonstrated the efficacy of the new method on a variety of 1- D test problems with different features, and demonstrated that the solutions produced retain sharp fronts, correct wave speeds, remain oscillation-free, are not subject to the wall-heating error, and maintain high-order accuracy.

A The WENO- $|u_x|$ and WENO-Noh schemes

For our numerical simulations, we use a variety of combinations of the WENO scheme, the C -method, the wall C -method, and the noise indicator. For the purpose of comparison, we implement two additional methods. The first is a classical artificial viscosity scheme, WENO- $|u_x|$, and the second is WENO-Noh, an artificial viscosity method introduced by Noh [37]. We will employ WENO-Noh primarily as a comparison for the wall C -method for shock-wall collision, while WENO- $|u_x|$ will serve as a benchmark for the usual C -method.

A.1 WENO- $|u_x|$: classical artificial viscosity

This is the classical artificial viscosity scheme, where viscosity is only added to the momentum equation and the localizing coefficient is given by $|\partial_x u|$. More precisely, we implement the method in the following manner:

$$\partial_t \rho + \partial_x(\rho u) = 0, \tag{39a}$$

$$\partial_t(\rho u) + \partial_x(\rho u^2 + p) = \partial_x \left((\Delta x)^2 \beta^u \rho |\partial_x u| \partial_x u \right), \tag{39b}$$

$$\partial_t E + \partial_x(uE + up) = 0. \tag{39c}$$

The time and spatial discretizations are done in as in §3.3. This scheme will serve primarily as a benchmark for WENO- C .

A.2 WENO-Noh: an artificial viscosity method of Noh

This artificial viscosity scheme of Noh [37] introduces an additional heat conduction term to the energy equation, in addition to the usual viscosity term in the momentum equation. For more details, we refer the reader to [37]. We implement the method in the following fashion: the equations of motion are

$$\partial_t \rho + \partial_x(\rho u) = 0, \tag{40a}$$

$$\partial_t(\rho u) + \partial_x(\rho u^2 + p) = \partial_x \left((\Delta x)^2 \beta_{\text{Noh}}^u \rho |\partial_x u| \partial_x u \right), \tag{40b}$$

$$\partial_t E + \partial_x(uE + up) = \partial_x \left((\Delta x)^2 \beta_{\text{Noh}}^E \rho |\partial_x u| \partial_x e \right). \tag{40c}$$

Here, $e = \frac{p}{(\gamma-1)\rho}$ is the specific internal energy of the system. The numerical discretization is then done in an identical fashion to that described in §3.3. We will employ this scheme with the aim of fully suppressing post-collision noise, even at the expense of a less accurate solution prior to shock-wall collision.

For readability, we will use Table 12 to refer to these various schemes.

Scheme	Description
WENO	standard fifth-order WENO procedure for the usual Euler equations.
WENO- $ u_x $	WENO scheme with classical artificial viscosity.
WENO-Noh	WENO scheme with Noh's artificial viscosity method.
WENO- C	WENO scheme with the C -method.
WENO- C - W	WENO scheme with the C -method and the wall C -method outlined in §3.
WENO- N	WENO scheme with the noise indicator outlined in §4.
WENO- C - N	WENO scheme with the C -method and the noise indicator.
WENO- W - N	WENO scheme with the wall C -method and the noise indicator.
WENO- C - W - N	WENO scheme with the C -method, the wall C -method and the noise indicator.
WENO- $\Delta^r u$	WENO scheme with linear hyperviscosity (38).

Table 12: Various numerical schemes used in the simulations.

B Calculation of the exact solution post shock-wall collision

In this section, we provide details for the calculation of the exact solution to Sod-type problem post shock-wall collision. The solution, calculated based on the Rankine-Hugoniot conditions (10) and the assumption that the post-shock velocity is identically zero both pre and post shock-wall collision, is valid until the reflected shock front collides with the contact wave. We assume for simplicity that the shock front is traveling to the right (so that the shock speed $\dot{\sigma}$ satisfies $\dot{\sigma}(t) > 0$ pre shock-wall collision) and collides with, and reflects back off of, the right boundary. We also assume that the shock $\sigma(t)$ separates two constant states, \mathbf{u}_l and \mathbf{u}_r , to the left and right of the shock, respectively.

The left states \mathbf{u}_l and the post-shock velocity $u_r = 0$ are all known; the unknowns are thus the post-shock density ρ_r , energy E_r (or, equivalently, pressure p_r), and shock speed $\dot{\sigma}(t)$. The R-H conditions (10b) and (10a) yield

$$p_r = \rho_l u_l^2 + p_l - \dot{\sigma} \rho_l u_l, \quad (41)$$

$$\rho_r = \rho_l - \frac{\rho_l u_l}{\dot{\sigma}}, \quad (42)$$

respectively, so it only remains to calculate the shock speed $\dot{\sigma}$. Substituting (41) into (10c)

and simplifying leads to a quadratic equation for $\dot{\sigma}$,

$$\dot{\sigma}^2 - \frac{1}{2}(3 - \gamma)u_l \dot{\sigma} - \frac{(\gamma - 1)(E_l + p_l)}{\rho_l} = 0,$$

which has solutions

$$\dot{\sigma} = \frac{1}{4}(3 - \gamma)u_l \pm \sqrt{\left(\frac{(3 - \gamma)u_l}{4}\right)^2 + \frac{(\gamma - 1)(E_l + p_l)}{\rho_l}}.$$

We take the negative root $\dot{\sigma} < 0$, since the shock moves to the left post shock-wall collision:

$$\dot{\sigma} = \frac{1}{4}(3 - \gamma)u_l - \sqrt{\left(\frac{(3 - \gamma)u_l}{4}\right)^2 + \frac{(\gamma - 1)(E_l + p_l)}{\rho_l}}. \quad (43)$$

The relations (41), (42), and (43) then provide the complete exact solution post shock-wall collision, up until the time that the reflected shock front collides with the contact discontinuity.

C Comparison of optimized-parameter runs with fixed-parameter runs

In this section, we compare the optimized-parameter runs presented in §5, with a set of runs using fixed parameters. The fixed-parameter runs have the C -equation parameters ε and κ take the fixed value 1, with the exception of ε_w , to which we assign the fixed value $\varepsilon_w = 50.0$. The artificial viscosity parameters β are still free to choose, and so vary from problem to problem. The particular choices of β for each test problem shown in the figures below are listed in the corresponding caption. For the initial data, we refer the reader to the relevant section in the main body of the paper.

We present results for the Sod shock-wall collision, Noh, LeBlanc shock-wall collision, Peak, and Osher-Shu shock-wall collision problems. In the figures shown below, Run 1 indicates the solution computed using the optimized set of parameters, while Run 2 indicates the solution computed using the fixed set of parameters.

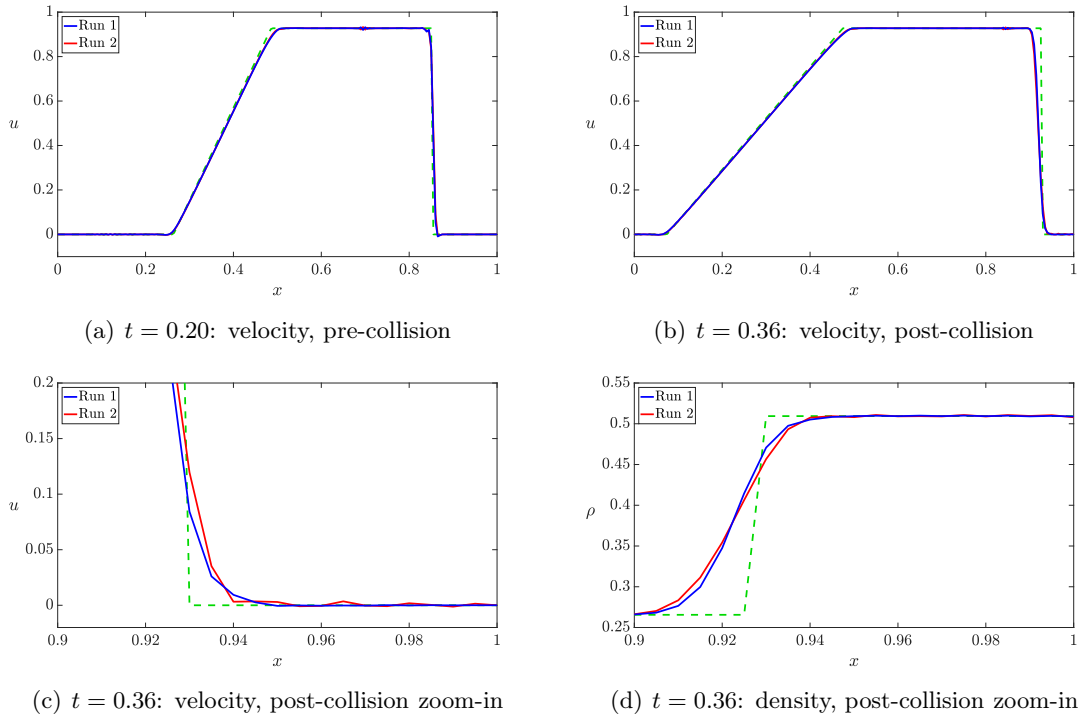


Figure 25: Comparison of the optimized-parameter and fixed-parameter WENO- C - W runs for the Sod shock tube problem before and after shock-wall collision. The artificial viscosity parameters for the fixed-parameter Run 2 are chosen as $\beta^u = 1.0$, $\beta^E = 0.0$, $\beta_w^u = 5.0$, $\beta_w^E = 10.0$.

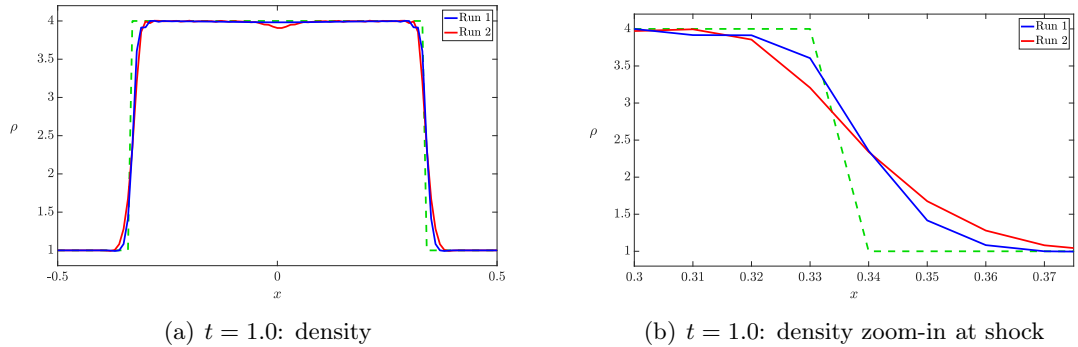


Figure 26: Comparison of the optimized-parameter and fixed-parameter WENO- C runs for the Noh problem. The artificial viscosity parameters for the fixed-parameter Run 2 are chosen as $\beta^u = 3.0$, $\beta^E = 30.0$.

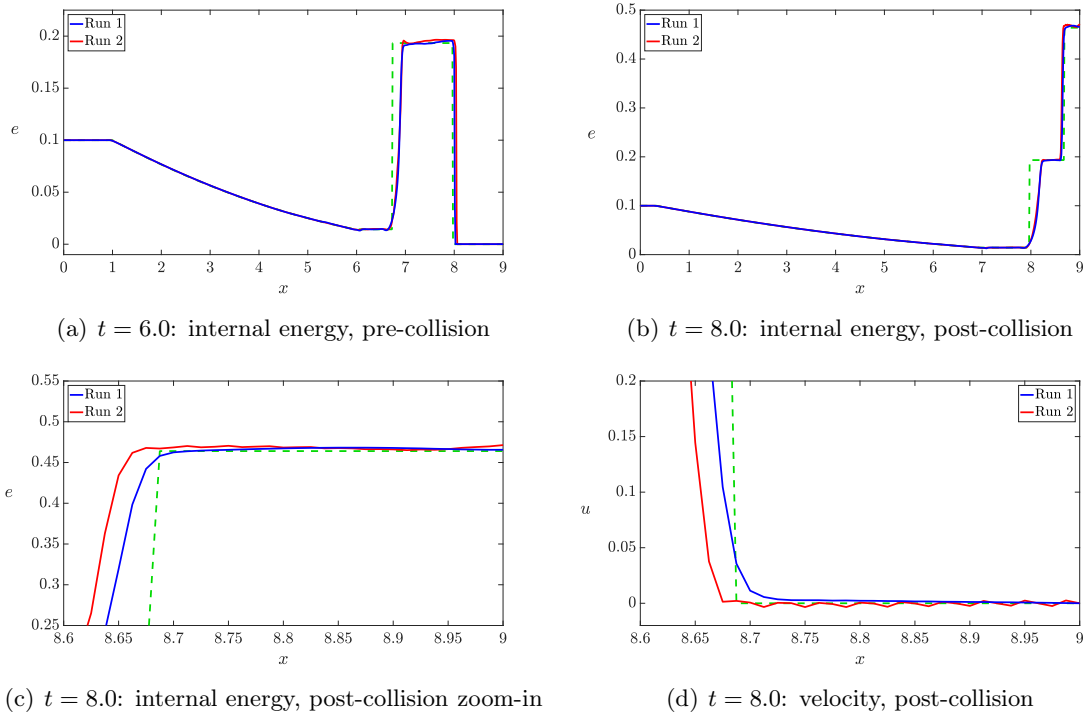


Figure 27: Comparison of the optimized-parameter and fixed-parameter WENO- C - W runs for the LeBlanc shock tube problem before and after shock-wall collision. The artificial viscosity parameters for the fixed-parameter Run 2 are chosen as $\beta^u = 0.001$, $\beta^E = 0.0$, $\beta^e = 0.5$, $\beta_w^u = 4.0$, $\beta_w^E = 15.0$, $\beta_w^e = 0.0$.

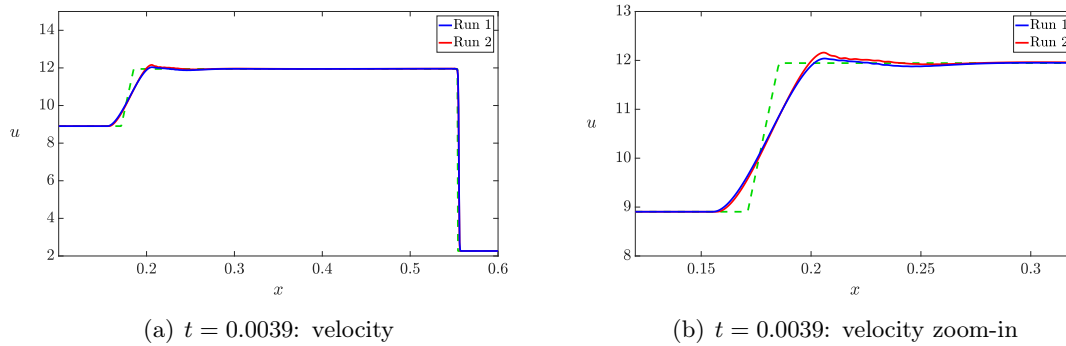


Figure 28: Comparison of the optimized-parameter and fixed-parameter WENO- C runs for the Peak shock tube problem. The artificial viscosity parameters for the fixed-parameter Run 2 are chosen as $\beta^u = 1.0$, $\beta^E = 0.0$, $\beta^r = 10.0$.

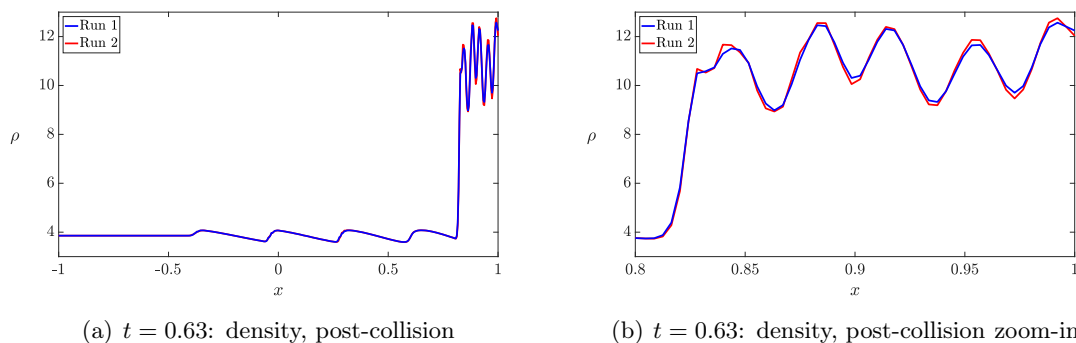


Figure 29: Comparison of the optimized-parameter and fixed-parameter WENO- $C-W$ runs for the Osher-Shu shock tube problem after shock-wall collision. The artificial viscosity parameters for the fixed-parameter Run 2 are chosen as $\beta^u = 1.0$, $\beta^E = 0.0$, $\beta_w^u = 2.5$, $\beta_w^E = 0.85$.

Acknowledgements

Research reported in this publication was supported by the Office of Defense Nuclear Non-proliferation Research and Development and by the Defense Threat Reduction Agency under Interagency Agreement number HDTRA1825370 (DTRA10027 – 25370) as work for others. SS was partially supported by DTRA HDTRA11810022.

We would like to express our gratitude to the anonymous referees for their numerous suggestions that have greatly improved the manuscript.

References

- [1] R. A. Alpher and R. J. Rubin. Normal reflection of shock waves from moving boundaries. *Journal of Applied Physics*, 25(3):395–399, 1954. 3.4
- [2] G. E. Barter and D. L. Darmofal. Shock capturing with PDE-based artificial viscosity for DGFEM: Part I, Formulation. *Journal of Computational Physics*, 229(5):1810–1827, 2010. 1.1
- [3] A. W. Cook and W. H. Cabot. A high-wavenumber viscosity for high-resolution numerical methods. *Journal of Computational Physics*, 195(2):594 – 601, 2004. 1.1, 4.4, 5.6.1
- [4] A. W. Cook and W. H. Cabot. Hyperviscosity for shock-turbulence interactions. *Journal of Computational Physics*, 203:379–385, 02 2004. 1.1, 5.6.1
- [5] E. J. Caramana, M. J. Shashkov, and P. P. Whalen. Formulations of artificial viscosity for multi-dimensional shock wave computations. *Journal of Computational Physics*, 144(1):70 – 97, 1998. 5.6.1
- [6] R. R. Coifman and D. L. Donoho. *Translation-Invariant De-Noising*, pages 125–150. Springer New York, New York, NY, 1995. 4

- [7] P. Colella. A direct Eulerian MUSCL scheme for gas dynamics. *SIAM Journal on Scientific and Statistical Computing*, 6:104–117, 1985. 1
- [8] P. Colella and P. R. Woodward. The numerical simulation of two-dimensional fluid flow with strong shocks. *Journal of Computational Physics*, 54:115 – 173, 1984. 1
- [9] P. Colella and P. R. Woodward. The piecewise parabolic method (PPM) for gas dynamical simulations. *Journal of Computational Physics*, 54:174 – 201, 1984. 1
- [10] R. Courant and K.O. Friedrichs. *Supersonic Flow and Shock Waves*. Applied Mathematical Sciences. Springer New York, 1999. 3.4
- [11] R. J. DiPerna. Convergence of the viscosity method for isentropic gas dynamics. *Communications in Mathematical Physics*, 91(1):1–30, Mar 1983. 1.1
- [12] R. Donat and A. Marquina. Capturing shock reflections: An improved flux formula. *Journal of Computational Physics*, 125(1):42 – 58, 1996. 3.4
- [13] M. Farge. Wavelet transforms and their applications to turbulence. In *Annual review of fluid mechanics, Vol. 24*, pages 395–457. Annual Reviews, Palo Alto, CA, 1992. 4
- [14] R. A. Gentry, R. E. Martin, and B. J. Daly. An Eulerian differencing method for unsteady compressible flow problems. *J. Computational Physics*, 1:87–118, 1966. 1.1
- [15] J. A. Greenough and W. J. Rider. A quantitative comparison of numerical methods for the compressible euler equations: Fifth-order weno and piecewise-linear godunov. *J. Comput. Phys.*, 196(1):259–281, May 2004. 1, 5, 5.2.4, 5.2.4, 5.2.5, 5.5
- [16] A. Harten, B. Engquist, S. Osher, and S. R. Chakravarthy. Uniformly high-order accurate essentially non-oscillatory schemes, III. *Journal of Computational Physics*, 71:231 – 303, 1987. 1
- [17] H. T. Huynh. Accurate upwind methods for the Euler equations. *SIAM Journal on Numerical Analysis*, 32:1565–1619, 1995. 1
- [18] O. Igra, G. Ben-Dor, G. Mazon, and M. Mond. Head-on collision between normal shock waves and a rubber-supported plate, a parametric study. *Shock Waves*, 2(3):189–200, Sep 1992. 3.4
- [19] G.-S. Jiang and C.-W. Shu. Efficient implementation of weighted ENO schemes. *J. Comput. Phys.*, 126(1):202–228, June 1996. 1, 3.3.1, 5.4.2
- [20] R. Landshoff. A numerical method for treating fluid flow in the presence of shocks. *Los Alamos National Laboratory Report, LA-1930*, 1 1955. 1.1, 5.6.1
- [21] A. Lapidus. A detached shock calculation by second-order finite differences. *Journal of Computational Physics*, 2:154 – 177, 1967. 1.1

- [22] Andrew Majda and Stanley Osher. Propagation of error into regions of smoothness for accurate difference approximations to hyperbolic equations. *Communications on Pure and Applied Mathematics*, 30(6):671–705, 1977. 1
- [23] B. Van Leer. Towards the ultimate conservative difference scheme. V. A second-order sequel to Godunov’s method. *Journal of Computational Physics*, 32:101 – 136, 1979. 1
- [24] R. J. LeVeque. *Finite Volume Methods for Hyperbolic Problems*. Cambridge Texts in Applied Mathematics. Cambridge University Press, 2002. 2.1
- [25] R. Liska and B. Wendroff. Comparison of several difference schemes on 1D and 2D test problems for the Euler equations. *SIAM J. Sci. Comput*, 25:995–1017, 2003. 1, 5.3, 5.5, 5.5
- [26] W. Liu, J. Cheng, and C.-W. Shu. High-order conservative Lagrangian schemes with Lax-Wendroff type time discretization for the compressible Euler equations. *Journal of Computational Physics*, 228:8872–8891, 2009. 5.4
- [27] X.-D. Liu and P. D. Lax. Solution of two-dimensional riemann problems of gas dynamics by positive schemes. *SIAM Journal on Scientific Computing*, 19(2):319–340, 1998. 5.5
- [28] X.-D. Liu and P. D. Lax. Positive schemes for solving multi-dimensional hyperbolic systems of conservation laws ii. *Journal of Computational Physics*, 187(2):428 – 440, 2003. 5.5
- [29] X.-D. Liu, S. Osher, and T. Chan. Weighted essentially non-oscillatory schemes. *Journal of Computational Physics*, 115:200–212, 1994. 1
- [30] R. Loubère and M. Shashkov. A subcell remapping method on staggered polygonal grids for arbitrary-Lagrangian-Eulerian methods. *Journal of Computational Physics*, 209:105–138, 2005. 5.4
- [31] L. G. Margolin. The reality of artificial viscosity. *Shock Waves*, Feb 2018. 1.1
- [32] A. E. Mattsson and W. J. Rider. Artificial viscosity: back to the basics. *Internat. J. Numer. Methods Fluids*, 77(7):400–417, 2015. 1.1
- [33] G. Mazor, O. Igra, G. Ben-Dor, M. Mond, H. Reichenbach, and F. T. Smith. Head-on collision of normal shock waves with a rubber-supported wall. *Phil. Trans. R. Soc. Lond. A*, 338(1650):237–269, 1992. 3.4
- [34] C. Meneveau. Analysis of turbulence in the orthonormal wavelet representation. *J. Fluid Mech.*, 232:469–520, 1991. 4
- [35] R. Menikoff. Errors when shock waves interact due to numerical shock width. *SIAM J. Sci. Comput.*, 15(5):1227–1242, 1994. 5.2.1
- [36] R. F. Meyer. The impact of a shock wave on a movable wall. *Journal of Fluid Mechanics*, 3:309–323, 1957. 3.4

- [37] W. F. Noh. Errors for calculations of strong shocks using an artificial viscosity and an artificial heat flux. *J. Comput. Phys.*, 72(1):78 – 120, 1987. 2.2, 3.4, 5.2.1, 5.2.2, 4, 5.3, A, A.2
- [38] T. Passot and A. Pouquet. Hyperviscosity for compressible flows using spectral methods. *Journal of Computational Physics*, 75(2):300 – 313, 1988. 5.6.1
- [39] J. J. Quirk. A contribution to the great Riemann solver debate. *Int. J. Num. Methods Fluids*, 18:555–574, 1994. 1
- [40] J. Reisner, J. Serenca, and S. Shkoller. A space-time smooth artificial viscosity method for nonlinear conservation laws. *J. Comput. Phys.*, 235:912–933, 2013. (document), 1, 1.4, 2.1, 2.2, 2.2, 5.4
- [41] R. Ramani, J. Reisner, and S. Shkoller. A space-time smooth artificial viscosity method with wavelet noise indicator and shock collision scheme, Part 2: the 2-D case. *Preprint*, 2018. (document), 1, 2
- [42] R. Ramani, J. Reisner, and S. Shkoller. A space-time smooth artificial viscosity method for shock-shock and shock-contact collision. *In preparation*. 3.4.2, 1
- [43] W. J. Rider. Revisiting wall heating. *J. Comput. Phys.*, 162(2):395 – 410, 2000. 2.2, 5.2.1
- [44] K. Schneider and O. V. Vasilyev. Wavelet methods in computational fluid dynamics. In *Annual review of fluid mechanics. Vol. 42*, volume 42 of *Annu. Rev. Fluid Mech.*, pages 473–503. Annual Reviews, Palo Alto, CA, 2010. 4
- [45] C.-W. Shu and S. Osher. Efficient implementation of essentially non-oscillatory shock-capturing schemes. *Journal of Computational Physics*, 77:439 – 471, 1988. 1
- [46] C.-W. Shu and S. Osher. Efficient implementation of essentially nonoscillatory shock-capturing schemes. II. *J. Comput. Phys.*, 83(1):32–78, 1989. 1, 5.6
- [47] C.-W. Shu. High-order finite difference and finite volume weno schemes and discontinuous galerkin methods for cfd. *International Journal of Computational Fluid Dynamics*, 17(2):107–118, 2003. 3.3.1
- [48] E. F. Toro. *Riemann solvers and numerical methods for fluid dynamics*. Springer-Verlag Berlin Heidelberg, 2009. 2.1
- [49] J. Von Neumann and R. D. Richtmyer. A method for the numerical calculation of hydrodynamic shocks. *J. Appl. Phys.*, 21:232–237, 1950. 1.1
- [50] M. L. Wilkins. Use of artificial viscosity in multidimensional fluid dynamic calculations. *Journal of Computational Physics*, 36(3):281 – 303, 1980. 1.1, 5.6.1